Fourier Analysis and Design of a Shielded 120 kW Inductive Wireless System

Andrew Foote, *Member, IEEE*, Daniel Costinett, *Senior Member, IEEE*, Ruediger Kusch, *Senior Member, IEEE*, Mostak Mohammad, *Senior Member, IEEE*, and Omer Onar, *Senior Member, IEEE*

***Abstract*—High-power inductive wireless power transfer (WPT) systems for electric vehicles are designed to meet specifications, such as stray field, power level, efficiency, misalignment tolerance, and ground clearance. These metrics are all heavily influenced by the coil geometry. This article proposes a coil design method based on the Fourier analysis method (FAM), which is an analytical method for directly designing coil geometries to meet stray field and power level requirements through an optimization of Fourier basis function coefficients. In this work, two 120 kW WPT proof-of-concept demonstrators with low stray field and high efficiency are built from FAM optimization results to validate the models and show the impact of the FAM design process. Experimental validation of the Generation 2 demonstrator at 120 kW output power resulted in a measured dc/dc efficiency of 97.2% at alignment with a 125 mm airgap. At the 120 kW test point, the stray fields 80 cm away from the center of the airgap between the coil assemblies were 3.4 μT(rms) on the *X*-axis and 3.5 μT(rms) on the *Y*-axis, much lower than the 27 μT(rms) ICNIRP limit.**

***Index Terms*—Coil design, electric vehicles (EVs), Fourier analysis, inductive power transmission, wireless power transfer (WPT).**

I. Introduction

INDUCTIVE wireless power transfer (WPT) for electric vehicles (EVs) has several advantages over conductive charging, including improvements in convenience, safety, automation, and vandalism resistance. Wireless charging systems can be completely hands-free with no moving parts or connectors exposed to the elements. With these benefits, WPT systems have been implemented in consumer homes, bus stops, docks, and warehouses with power levels from 3 to 300 kW [1]. Many of the current implementations of high-power wireless systems are for electric buses, which use WPT for opportunity-charging. Frequent charging allows electric buses to have smaller and less expensive batteries compared to those that must have enough range for an entire shift without charging. These WPT systems often use many vehicle assemblies (VAs) on the underside of buses paired with multiple ground assemblies (GAs) in parallel to achieve high power levels, each limited to a power of around 50–75 kW [2], [3].

Meanwhile, the power levels of conductive dc fast-charging continue to increase and are exceeding 120 kW or even 270 kW for passenger EVs [4]. For these EVs, the onboard components of the wireless charger must fit within smaller wheelbases and track widths such that multiple VAs may not be acceptable and power density is more critical. The airgaps for passenger EVs, which often range from 125 to 250 mm depending on the ground clearance, may also be larger than those of buses that are able to kneel at stops, reducing ground clearance to 100–175 mm. As summarized in the SAE J2954 standard [5], EV wireless chargers must meet requirements, such as stray field safety limits, thermal limits, misalignment tolerance, interoperability, efficiency, and others, that depend heavily on the coil geometry. In particular, meeting the 27 μT(rms) ICNIRP 2010 public exposure magnetic field limit [6] or the 15 μT(rms) recommended limit for pacemakers at the nominal WPT frequency of 85 kHz [5] at the edge of the vehicle (typically approximated at 80 cm from the center of the VA coil) and the radiated EMI field limits in CISPR 11 [7] has been difficult even for 11 kW systems [8]. In addition, large coil temperature increases have been seen in 11 kW systems [9] motivating active cooling, such as in the liquid cooled enclosure of [10]. Therefore, most commercial inductive WPT systems for passenger vehicles have been limited to 22 kW or lower [2], [3]. This clear limitation relative to conductive dc fast-charging has led to many efforts to increase the power density and efficiency of inductive WPT systems while limiting the stray fields of the system, and research demonstrations of up to 120 kW have been performed in single VA and GA systems [11], [12].

In Table I, high power systems in the literature are compared with the Generation 2 (Gen. 2) 120 kW demonstrator of this work. In this table, two comparison metrics are used to compare works at different power level and airgaps: the airgap divided by the geometric mean length (GML) of the coil extents

Manuscript received 13 December 2023; revised 22 March 2024 and 21 May 2024; accepted 28 June 2024. Date of publication 15 July 2024; date of current version 11 September 2024. This work was funded by Volkswagen Group Innovation in collaboration with the CURENT Engineering Research Center at the University of Tennessee, Knoxville and the Power Electronics and Electric Machinery Research Center at Oak Ridge National Laboratory. Recommended for publication by Associate Editor D. Qiu. *(Corresponding author: Andrew Foote.)*

Andrew Foote is with Volkswagen Group of America, Knoxville, TN 37920 USA (e-mail: afoote5@vols.utk.edu).

Daniel Costinett is with the Department of Electrical Engineering and Computer Science, University of Tennessee, Knoxville, TN 37996 USA.

Ruediger Kusch is with Volkswagen Group Components, 38436 Wolfsburg, Germany.

Mostak Mohammad and Omer Onar are with Oak Ridge National Laboratory, Knoxville, TN 37932 USA.

Color versions of one or more figures in this article are available at https://doi.org/10.1109/TPEL.2024.3427635.

Digital Object Identifier 10.1109/TPEL.2024.3427635

TABLE I
REVIEW OF STATIONARY HIGH-POWER WPT SYSTEMS

Institute/ Company	Power Level	Airgap (mm)	Coil Dimensions (Airgap/GML)	Stray Field RMS at 0.8 m - X, Y ($kW^{0.5}/\mu T(rms)$)	Efficiency	Freq. (kHz)	Coil Shape	VA Power Density
This Work Gen. 2 Demonstrator	**120 kW**	**125**	**0.420 m × 0.540 m (0.262)**	**3.4 µT, 3.5 μT (3.2, 3.1)**	**97.2% DC/DC**	**89**	**Shielded DD**	**530 kW/m^2 4.1 kW/kg**
ETH Zurich [16], [17]	50 kW	160	0.760 m × 0.410 m (0.286)	N/A, 22.5μT (N/A, 0.31)	95.8% DC/DC	85	Rect.	160 kW/m^2 2.0 kW/kg
ETH Zurich [16], [17]	50 kW	160	0.760 m × 0.410 m (0.286)	N/A, 12.5 μT (N/A, 0.57)	95.3% DC/DC	85	DD	160 kW/m^2 2.0 kW/kg
Warwick [18]	50 kW	200	0.75 m × 0.3 m (0.422)	N/A	89% System	85	DD	222 kW/m^2
Utah State [19]	125 kW	300	1.320 m × 1.480 m (0.215)	N/A	93% DC/DC	85	Rect.	64 kW/m^2
Auckland [20]	50 kW	210	0.620 m × 0.605 m (0.343)	At (7.5 cm, 10 cm) N/A, 28.6 μT (N/A, 0.25)	At (7.5 cm, 10 cm) 93.7% DC/DC	85	Rect.	133 kW/m^2
ORNL (DD) [11], [15]	120 kW	125	0.876 m × 0.673 m (0.163)	At 11 kW 19.1 μT, 12.3 µT (0.17, 0.27)	97.1% DC/DC	25	DD	203 kW/m^2 2.28 kW/kg*
ORNL (3Φ) [21]	50 kW	150	0.544 m × 0.471 m (0.296)	N/A, 34.7μT (N/A, 0.20)	95.1% DC/DC	85	3Φ-DD	195 kW/m^2 3.65 kW/kg*

*These works do not include the weight of their resonant components in their reported weights.

(Airgap/GML) and the square root of the output power divided by the magnetic stray field measured at 0.8 m [$kW^{0.5}/\mu T$ (rms)]. In inductive WPT systems, the fields generated by the coils decay rapidly across the airgap at a rate inversely proportional to the coil area. Comparisons of the efficiency and coil sizes of systems must consider their airgaps as also proposed in [13] and [14]. The GML is defined as GML $= \sqrt{x_{\text{dim}} y_{\text{dim}}}$ where x_{dim} and y_{dim} are the rectangular dimensions of the coil. For example, the GML of the Generation 1 (Gen. 1) and Gen. 2 demonstrators, with dimensions of 42 cm × 54 cm, is 47.6 cm resulting in an airgap/GML ratio of 0.262 at a 125 mm airgap. Likewise, stray fields are a function of the total amp-turns of the coil structure [15]; therefore, the stray field and power level are compared by dividing the square root of the output power level by the stray field at 80 cm from the center of the VA coil. The stray field metric $kW^{0.5}/\mu T$(rms) comes from the direct relationship between the coil currents and field magnitude and the coil to coil power equation, $P = \omega M I_1 I_2$, where the power is proportional to the product of the coil currents. This relationship allows the stray fields of systems operating at different power levels to be compared and for the scaling of stray field measurements to higher or lower power levels. The power density of systems in terms of coupler-area and gravimetric power density is also compared, where the gravimetric power density includes weight of the VA coil assembly with the capacitor bank, but without the rectifier or onboard DC/DC as given in most publications. Note that some publications in Table I do not include capacitor banks in their reported weights. The area-related power density depends on the airgap, as smaller coil areas are possible as the airgap decreases assuming the same airgap/GML ratio. The coupler-area power densities of lower-power systems are also often lower than higher-power systems as the areas of the coils are sized with respect to the airgap to achieve acceptable coupling and efficiency.

As seen, the works in the literature have a power density up to around 200 kW/m^2 and 2.0 kW/kg. The stray field performance of these systems are also of concern, especially with increasing power level. For a 120 kW system, a stray field performance of 0.4 $kW^{0.5}/\mu T$(rms) is needed meet the ICNIRP 2010 27 μT(rms) stray field standard in the 85 kHz frequency band at 80 cm from the center of the VA coil. For the 15 μT(rms) limit given for pacemaker compatibility [5], the value is 0.7 $kW^{0.5}/\mu T$(rms). The highest value in the reviewed systems was 0.57 $kW^{0.5}/\mu T$(rms) for the Double-D or bipolar geometry of [17], but this was measured on the short-axis of the geometry, where the stray field for the bipolar geometry is minimized [22] and the long-axis stray field at 0.8 m is not reported. Adding extended layers of shielding materials such as ferrite for bipolar coils [15] or aluminum for unipolar coil geometries has been shown to decrease the stray field to some extent [22], but only as a percentage of the stray field of the coil geometry itself as also previously analyzed for geometries generated by the Fourier analysis method (FAM) in [23].

This work aims to improve these metrics with a proof-of-concept demonstrator that achieves a power density of 530 kW/m^2 and 4.1 kW/kg including the compensation capacitor bank in a shielded bipolar geometry integrated with liquid cooling. Achieving higher power levels and power density required improvements in thermal, mechanical, and magnetic performance. To assess the tradeoff of stray field and total current in the coil, the FAM optimization approach of Foote et al. [23] was used to generate a shielded bipolar geometry. Using this geometry, a Gen. 1 demonstrator was designed, built, and tested, and then a Gen. 2 version was made to improve on the first, yielding a dc/dc efficiency of 97.2% at 120 kW output. At 120 kW, the measured stray field at 80 cm was 3.4 and 3.5 μT(rms) on the *X*- and *Y*-axes, respectively, for a stray field performance of 3.2 and 3.1 $kW^{0.5}/\mu T$(rms) at a 125 mm airgap.

To achieve this performance, this work applies the FAM optimization detailed in [23] to design the bipolar coil geometry of the 120 kW WPT demonstrators. The FAM design approach has already been successfully validated in the design and measurement of a shielded, unipolar 6.6 kW system [23]. In [23], the FAM was used to flexibly generate and analyze many coil geometry types and aspect ratios with rapid computational speeds and compared to finite-element analysis (FEA)-based methods. This work validates the FAM approach at higher power levels and with different design inputs than previous work, resulting in an optimized bipolar geometry. This is implemented in an experimental demonstrator with higher efficiency, power density, and lower stray field than the literature systems reviewed in Table I.

In the FAM, Fourier basis function coefficients are optimized to produce optimized shielded coil geometries with minimized loss metrics under stray field, coil dimension, and power level constraints. Implementing one of these geometries produces a system with lower stray field and high efficiency in the target coil dimensions. To implement the geometry, loss modeling is used to inform the choice of ferrite thicknesses, conductor size, and estimate cooling requirements. The calculation of the ferrite and external proximity effect loss is aided by the Fourier representation of the coil geometry.

The rest of this article is organized as follows. Section II details the FAMfor coil geometry optimization, loss models, the material selection tradeoff, and thermal modeling for the 120 kW demonstrator design. In Section III, the construction and testing of the Gen. 1 demonstrator are presented with the discussion of improvements in the lead passthroughs to reduce circulating flux, the ferrite tile layout to reduce flux concentrations, and the encapsulant to reduce mechanical stress in the Gen. 2 demonstrator. To validate the design, the experimental validation of the Gen. 2 120 kW demonstrator is given in Section IV. Finally, Section V concludes this article.

II. Geometry Optimization and Design of a 120 kW Shielded Coil Assembly

A. Fourier Geometry Optimization

As detailed in [23], the FAM is an analytical method to directly design coil geometries through an optimization of Fourier basis function coefficients to meet specifications, such as power level, coil dimension, and stray field. The use of Fourier basis functions allows for the rapid computation of the currents, field, and coupling of a wide range of symmetric coil shapes. The outputs of the optimization are magnetic scalar potentials of coil geometries bounded to specified dimensions that meet the power and stray field constraints at given distances with minimum current, which is used as a loss factor metric. This first optimization step of the FAM design process in Fig. 1(a) is an inverse design step that directly optimizes the coil geometry from the input parameters. This optimization uses the coil dimension constraints x_{ext} and y_{ext} and a stray field constraint $B_{\text{str,lim}}$ at measurement extents x_{meas} and y_{meas} as illustrated in Fig. 2. Afterward, the number of turns is added to the Litz wire sizes and types and ferrite thickness to calculate

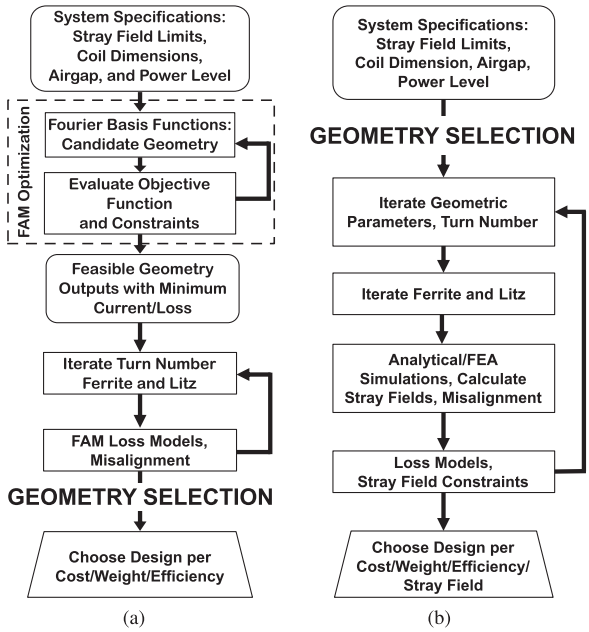

Fig. 1. Comparison of the FAM design process and a conventional design process. (a) FAM design process where complex coil geometries are generated to meet the stray field limit with minimum current or loss factors through an optimization of Fourier basis function coefficients. The number of turns and coil materials are then iterated over misalignment to evaluate loss for the candidate geometries and the final design coil geometry for implementation is chosen based on overall performance. (b) Conventional design process similar to [17], [24], [25] where geometric parameters are chosen and swept using FEA or analytical methods. Each parameter combination is evaluated for stray field and loss.

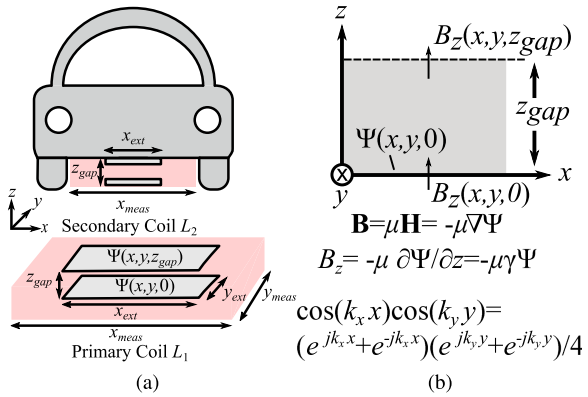

Fig. 2. (a) Illustration of the EV WPT system defined by coil outer dimensions of x_{ext} and y_{ext}, system airgap z_{gap}, stray field limits outside a region with dimensions of x_{meas} and y_{meas}, and magnetic scalar potential Ψ used in the FAM. (b) FAM axes layout and key equations.

the losses over misalignment for each of the four basis function types. These can be unipolar, bipolar, or even quadrupole geometries. Finally, the geometry, number of turns, and Litz and ferrite sizing is chosen for implementation of the demonstrator based on the overall performance of all the candidate designs. This is different from most conventional design processes summarized in Fig. 1(b), which are based on brute-force iterations in a predetermined geometry.

In the FAM, the four different basis functions used are combinations of cosine and sine functions in the X and Y directions: the $\cos x \cos y$, $\sin x \cos y$, $\cos x \sin y$, and $\sin x \sin y$ functions. The $\cos x \cos y$ set corresponds to circular or rectangular geometries, the $\sin x \cos y$ and $\cos x \sin y$ sets correspond to bipolar geometries, and the $\sin x \sin y$ set corresponds to quadrupole geometries. Each function is defined by k_x and k_y, the spatial wavenumbers in units of radians per meter in the X and Y directions, respectively, with cooresponding matrix coefficients, $\psi(m,n)$. These wavenumbers are $k_x(m) = 2\pi m/D_x$ and $k_y(n) = 2\pi n/D_y$ for integers m and n from $-N+1$ to $N-1$, where D_x and D_y are design space dimensions greater than the desired coil extents. The symmetry of the functions allows each geometry to be represented as an $N \times N \times 1$ matrix of coefficients representing the combinations of wavenumbers as detailed in [23]. The magnetic scalar potential in the spatial domain, $\Psi(x,y,z)$, is the inverse Discrete Fourier Transform of this matrix expressed by

$$\Psi(x,y,z) = \sum_{m,n=-N+1}^{N-1}\sum^{N-1} \psi(m,n)e^{j(k_x x+k_y y+k_z z)}/4. \quad (1)$$

For ferrite-backed coils, the potential of the coil surface is defined by the surface current boundary condition

$$\boldsymbol{K} = \nabla \times \hat{k}\Psi = \frac{\partial \Psi}{\partial y}\hat{i} - \frac{\partial \Psi}{\partial x}\hat{j} \quad (2)$$

where $\hat{i}$, $\hat{j}$, and $\hat{k}$ are unit vectors in the X, Y, and Z directions, respectively. This assumes that the change in the magnetic potential and field in the ferrite are close to zero from the low reluctance of the ferrite compared to the airgap. The surface currents in the X and Y directions, K_x and K_y, are then

$$K_x(x,y,0) = \sum_{m,n=-N+1}^{N-1}\sum^{N-1} jk_y\psi(m,n)e^{j(k_x x+k_y y)}/4 \quad (3)$$

$$K_y(x,y,0) = \sum_{m,n=-N+1}^{N-1}\sum^{N-1} -jk_x\psi(m,n)e^{j(k_x x+k_y y)}/4. \quad (4)$$

This surface current representation allows for the coil geometry to be analyzed as a surface current density independent from the number of turns N_T. To implement the geometry after the optimization, the current density is grouped into discrete conductor paths by following constant-value contours of the potential as detailed in [23].

In the Fourier domain, the potential Ψ is easily differentiated to obtain algebraic relationships between the potential and the field $\boldsymbol{B}$

$$\boldsymbol{B} = \mu_0 \boldsymbol{H} = -\mu_0 \nabla \Psi. \quad (5)$$

With no currents in the airgap in magnetostatic conditions, the field and potentials satisfy

$$\nabla^2 \Psi = \nabla^2 \boldsymbol{B} = 0 \quad (6)$$

which means the wavenumbers have the relationship

$$k_x^2 + k_y^2 + k_z^2 = 0. \quad (7)$$

When real, nonzero wavenumbers exist in the X and Y directions, the wavenumber in the Z direction, k_z, is

$$k_z = \pm\sqrt{-k_x^2 - k_y^2} = \pm j\gamma \quad (8)$$

where $\gamma = \sqrt{k_x^2 + k_y^2}$. Therefore, the fields in the airgap at z are a function of z_{gap} and γ for ferrite-backed coils and are

$$B_x(x,y,z) = \sum_{m,n=-N+1}^{N-1}\sum^{N-1} \frac{-\mu_0 jk_x\psi(m,n)e^{j(k_x x+k_y y)}}{4} \cdot \frac{\sinh\gamma(z-z_{\text{gap}})}{\sinh\gamma z_{\text{gap}}} \quad (9)$$

$$B_y(x,y,z) = \sum_{m,n=-N+1}^{N-1}\sum^{N-1} \frac{-\mu_0 jk_y\psi(m,n)e^{j(k_x x+k_y y)}}{4} \cdot \frac{\sinh\gamma(z-z_{\text{gap}})}{\sinh\gamma z_{\text{gap}}} \quad (10)$$

$$B_z(x,y,z) = \sum_{m,n=-N+1}^{N-1}\sum^{N-1} \frac{-\mu_0 \gamma\psi(m,n)e^{j(k_x x+k_y y)}}{4} \cdot \frac{\cosh\gamma(z-z_{\text{gap}})}{\sinh\gamma z_{\text{gap}}}. \quad (11)$$

The computation of the field at the surface of the coils allows for the computation of the coupling coefficient as detailed in [23] assuming matched couplers and currents

$$k = \frac{E_m(\psi)}{2E_s(\psi)} = \frac{MI_1I_2}{\frac{1}{2}L_1I_1^2 + \frac{1}{2}L_2I_2^2} = \frac{\int_\Omega \Psi(x,y,0)B_z(x,y,z_{\text{gap}})d\Omega}{\int_\Omega \Psi(x,y,0)B_z(x,y,0)d\Omega}. \quad (12)$$

The average of the fields in the airgap are also conveniently obtained by this representation. The average field is derived by integrating the contribution from each basis function from $z = 0$ to z_{gap} and dividing by z_{gap} to obtain the average field in the airgap

$$B_{x,\text{avg}}(x,y) = \sum_{m,n=-N+1}^{N-1}\sum^{N-1} \frac{-\mu_0 jk_x\psi(m,n)e^{j(k_x x+k_y y)}}{\gamma z_{\text{gap}}\sinh\gamma z_{\text{gap}}} \cdot (\cosh\gamma z_{\text{gap}} - 1) \quad (13)$$

$$B_{y,\text{avg}}(x,y) = \sum_{m,n=-N+1}^{N-1}\sum^{N-1} \frac{-\mu_0 jk_y\psi(m,n)e^{j(k_x x+k_y y)}}{\gamma z_{\text{gap}}\sinh\gamma z_{\text{gap}}} \cdot (\cosh\gamma z_{\text{gap}} - 1) \quad (14)$$

$$B_{z,\text{avg}}(x,y) = \sum_{m,n=-N+1}^{N-1}\sum^{N-1} \frac{-\mu_0 \gamma\psi(m,n)e^{j(k_x x+k_y y)}}{\gamma z_{\text{gap}}}. \quad (15)$$

The average field magnitude in the airgap, $B_{\text{avg}}(x,y)$, is then

$$B_{\text{avg}}(x,y) = \sqrt{B_{x,\text{avg}}(x,y)^2 + B_{y,\text{avg}}(x,y)^2 + B_{z,\text{avg}}(x,y)^2}. \quad (16)$$

Using this FAM framework, an optimization is formulated and solved to design coil geometries to minimize the loss factor $\Gamma^2_{K,\text{Loss}}$ for a fixed power level P when bounded by coil extents at x_{ext} and y_{ext} and field limits at the measurement extents x_{meas} and y_{meas} by $B_{\text{str,max}}(\psi)$

$$\min\left(\frac{\Gamma^2_{K,\text{Loss}}(\psi)}{P}+\alpha\frac{||\psi||_1}{P}\right)$$

s.t.

$$(P-2\pi f E_m(\psi))/P\le 0,$$

$$(B_{\text{str,max}}(\psi,x_{\text{meas}},y_{\text{meas}})-B_{\text{str,lim}})/B_{\text{str,lim}}\le 0,$$

$$\frac{\kappa^2_{\text{str}}(\psi,x_{\text{ext}},y_{\text{ext}})}{\Gamma^2_{K,\text{Loss}}(\psi)}-\beta\le 0. \tag{17}$$

$\Gamma_{K,\text{Loss}}(\psi)$ is a loss factor that corresponds with the total current magnitude in the coil geometry

$$\Gamma^2_{K,\text{Loss}}(\psi)=\int_\Omega K(x,y,0)^2 d\Omega$$
$$=\left(||K_x(\psi)||_2^2+||K_y(\psi)||_2^2\right)/16. \tag{18}$$

The 1-norm of the magnitude of the basis function coefficients is multiplied by $\alpha=0.1$, normalized by power, and added to the objective function to eliminate zero-valued basis functions, such as $\sin 0\cos y$, with a smaller weight than the normalized loss factor objective.

$B_{\text{str,max}}(\psi)$ is the stray maximum average stray field magnitude at x_{meas} and y_{meas}

$$B_{\text{str,max}}(\psi,x_{\text{meas}},y_{\text{meas}})=||B_{\text{str,avg}}(x,y)||_{50}. \tag{19}$$

The inclusion of stray field as a constraint incorporates the need for compliance with safety standards for public magnetic field exposure and EMI standards. $B_{\text{str,max}}(\psi,x_{\text{meas}},y_{\text{meas}})$ is computed as the 50-norm, which approximately the infinity norm or maximum, of the spatial stray-field matrix, $B_{\text{str,avg}}$. It was found that using the 50-norm instead of the maximum helped with the numerical convergence of the optimization. $B_{\text{str,avg}}$ is the average field magnitude over the Z direction of the airgap B_{avg} as in (16) outside the measurement extents x_{meas} and y_{meas}. The use of the average or 1-norm of the field across the airgap in the Z direction accounts for the stray fields in the entire airgap, such as near the surface of the primary coil, in the middle of the airgap, and at the surface of the other coil across the airgap.

The third constraint limits the current density to the desired coil extents such that the surface integral of the stray current squared $\kappa^2_{\text{str}}(\psi,x_{\text{ext}},y_{\text{ext}})=\int_\Omega K_{\text{str}}(x,y,0)^2 d\Omega$ outside the coil extents x_{ext} and y_{ext}, is a small percentage, $\beta=10^{-4}$ of the surface integral of the total current squared $\Gamma^2_{K,\text{Loss}}(\psi)$

$$\frac{\kappa^2_{\text{str}}(\psi,x_{\text{ext}},y_{\text{ext}})}{\Gamma^2_{K,\text{Loss}}(\psi)}-\beta\le 0. \tag{20}$$

B. Fourier Optimization Outputs

The FAM optimization of this work considers coil extents of $x_{\text{ext}}=0.4$ m and $y_{\text{ext}}=0.5$ m and a range of stray field limits $B_{\text{str,lim}}$ at measurement extents of $x_{\text{meas}}=0.6$ m and $y_{\text{meas}}=0.6$ m as labeled with boxes in Fig. 3. The airgap is $z_{\text{gap}}=0.21$ m and the power level is $P=120$ kW as summarized in Table II. This choice of coil and measurement extents results in an area-related power density of around 600 kW/m^2 with shielding equally in the X and Y directions. The overall design targets for the 120 kW demonstrators are summarized in Table III. The fmincon optimization algorithm from MATLAB was used to generate the outputs as done previously in [23]. The optimization outputs are shown in Fig. 3. Here, the outputs from the $\cos x\sin y$ basis function, which are bipolar geometries oriented in the Y direction, have the lowest current to achieve 120 kW with $B_{\text{str,lim}}$ below 300 μT. Compared to the optimization result of [23] where bipolar geometries were optimal only below 100 μT, the higher 120 kW power level, 40 cm $\times$ 50 cm coil extents with long length in the Y direction, and equal measurement extents result in the optimality of the Y direction bipolar geometry over unipolar geometries at higher stray field limits. More shielding is required to achieve low stray field at high power. The candidate geometry

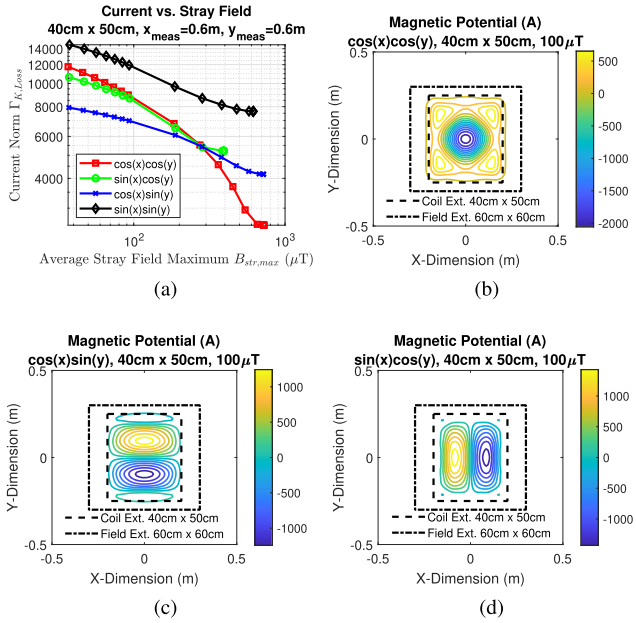

Fig. 3. FAM optimization for the 120 kW demonstrators. (a) Sweep of the basis functions for 120 kW design using the parameters $x_{\text{ext}}=0.4$ m and $y_{\text{ext}}=0.5$ m (labeled "Coil Ext." with dashed box), $x_{\text{meas}}=0.6$ m and $y_{\text{meas}}=0.6$ m (labeled "Field Ext." with dotted box), $z_{\text{gap}}=0.21$ m, and $P=120$ kW. Scalar potential contours of the (b) $\cos x\cos y$, (c) $\cos x\sin y$, and (d) $\sin x\cos y$ outputs with $B_{\text{str,avg}}=100$ μT and 14 turns.

TABLE II
FAM OPTIMIZATION PARAMETERS FOR THE 120 KW DEMONSTRATORS

FAM Optimization Parameters	Value
Power Level	$P=120$ kW
Stray Field Limit	$B_{\text{str,lim}}=5$ μT to 1 mT
Field Measurement Extents	$x_{\text{meas}}=0.6$ m and $y_{\text{meas}}=0.6$ m
Coil Extents	$x_{\text{ext}}=0.4$ m and $y_{\text{ext}}=0.5$ m
Airgap	$z_{\text{gap}}=0.21$ m

TABLE III
DESIGN TARGETS FOR THE 120 KW DEMONSTRATORS

Design Target	Value
Peak Power Level	120 kW
Inverter Input Voltage	$\leq$ 900 V
Battery Voltage Range	600-820 V
DC/DC Efficiency	$\geq$ 95%
Maximum Stray Fields at 0.8 m	$\leq$ 27 μT(rms)
Power Density	$\geq$ 250 kW/m^2 $\geq$ 4 kW/kg
Airgap	125 mm
Misalignment Tolerance	+/- 10 cm (X-axis) +/- 5 cm (Y-axis)

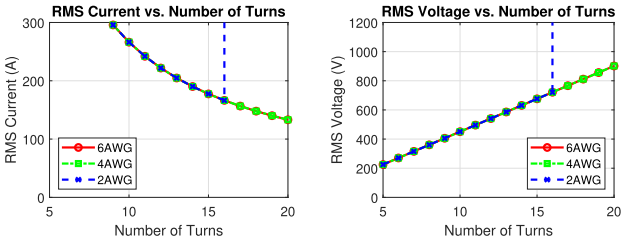

(a) (b)

Fig. 4. Effect of the number of turns on the (a) nominal rms current and (b) voltages at 120 kW output power, 125 mm airgap, and alignment for the $\cos x \sin y$ output at $B_{\text{str,avg}}$ =100 μT.

is chosen as the $\cos x \sin y$ output for $B_{\text{str,lim}} = 100$ μT as in Fig. 3(c). This geometry is similar to the conventional double-D or bipolar coil geometry, but has additional side turns on the longer dimension, which provide additional shielding on that axis where the stray fields tend to be higher [22].

After the geometry is chosen from the optimization outputs, it is discretized into a number of turns. The optimization is done with an airgap of $z_{\text{gap}} = 0.21$ m, but the target airgap of $z_{\text{gap}} = 0.125$ m, as in Table III, is used in the choice of the number of turns. The maximum coupling at alignment at this airgap sets the upper limit of the input impedance of the demonstrator, which is constrained by the inverter voltage rating. The bipolar geometry also requires an even number of turns. The impact of the number of turns on the nominal current and voltage at unity gain with an airgap of 125 mm at alignment is plotted in Fig. 4. Here, 14 turns supports efficient operation at the nominal 120 kW power level with 1.2 kV rated switching devices with a $\leq$ 900 Vdc inverter dc-link voltage and near-unity voltage gain operation near the upper end of the 600–820 Vdc battery voltage range. The input and output voltages at unity gain lower at larger airgaps or with misalignment.

C. Loss Modeling and Simulation Framework

With the geometry from the FAM optimization, loss modeling is performed to design a physical demonstrator. The loss models use a combination of calculated resistances, inductances, and ferrite loss derived from the FAM optimization and measured values to include the effect of the leads on the overall system

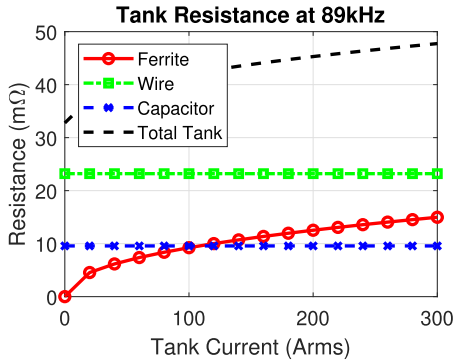

Fig. 5. Modeled series resistance values used in the PLECS simulations at 89 kHz.

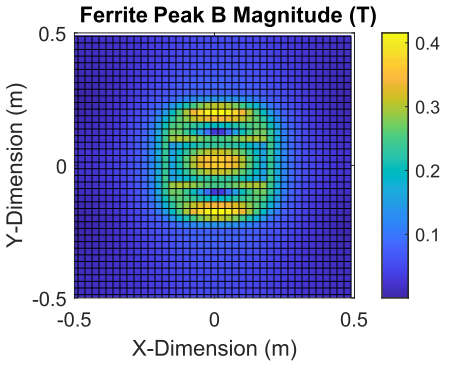

(a)

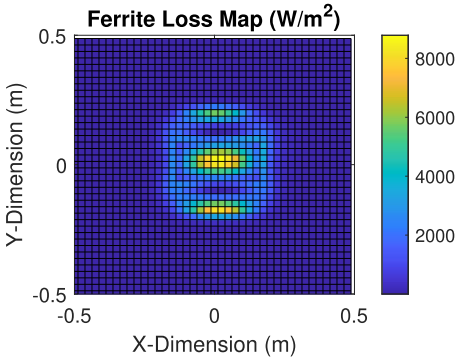

(b)

Fig. 6. FAM loss modeling of the Gen. 2 120 kW demonstrator ferrite at maximum misalignment with the modeled worst-case losses at 120 kW, which sums to around 800 W of ferrite loss over the coil area. The outer area has a ferrite thickness of 5 mm and the inner region has a thickness of 10 mm. (a) Peak ferrite flux density. (b) Ferrite loss density.

performance. These values are imported as lookup tables within the PLECS by Plexim circuit simulation software. The simulation used a 3-D lookup table of the modeled mutual inductance values as a function of X- and Y-axes misalignment and airgap inputs and the modeled self-inductance calculated by the Fourier representation of the coils as in [23].

The loss modeling approach previously detailed in [23] was used to model the losses of the demonstrator. These loss models calculate skin effect, proximity effect, and ferrite hysteresis

TABLE IV
LOSS MODEL PARAMETER DESCRIPTIONS AND VALUES

Parameters		Value
Ferrite Steinmetz Parameters Ferroxcube 3C95 20–150 kHz		$\mu_r = 3000$ $C_m = 92.1\text{e-}3$ mW/cm^3 $\alpha = 1.045$; $\beta = 2.440$ $C_{t0} = 1.332$; $C_{t1} = 0.0079$; $C_{t2} = 4.62\text{e-}5$
Temperature of Ferrite		$T_{fer} = 19$°C
Ferrite Thickness		$t_{fer} = 5$ mm (outer) $t_{fer} = 10$ mm (inner), 307mm x 130mm
Litz Wire 4 AWG/42	Outer Diameter Number of Strands Strand Diameter Cabling Operations Wire Length	$d_{out} = 8$ mm $n = 6750$ $d_{str} = 0.0635$ mm $N_b = 2$ $N_c = 1$ $L_T = 11.9$ m
Measured Lead Inductance and Resistance		$L_{lead} = 1.465\mu$H, $R_{lead} = 5$ mΩ, 89 kHz 24 mΩ, 267 kHz 55 mΩ, 445 kHz 102 mΩ, 623 kHz 163 mΩ, 801 kHz 235 mΩ, 979 kHz
Inverter Parameters CAS325M12HM2 Module Gate Drive Board CGD1700HB3P-HM3		$R_{DS} = 4$ mΩ $C_{oss} = 1.54$ nF $t_{dt} = 600$ ns $V_{GS} =$ -4/+15 V
Rectifier Device Curve Fit BSM300D12P2E001 Module Diode		$V_f = 0.9$ V $R_f = 3$ mΩ
Heatsink (HS) Thermal Resistance Coolant (Liq.) Temperature		0.014 (HS/Liq.)+ 0.035 (Case/HS ROHM) °C/W 25°C
Copper Wire Resistivity at 20°C		$\rho_{Cu} = 1.724\text{e-}8$ Ω-m
Temperature Coefficient, Copper		$C_{Cu,t} =$ +0.393 %/°C
Temperature of Copper		$T_{Cu} = 40$ °C
Gap Between Ferrite and Wire Planes		$z_g = 6.5$ mm
Compensation Capacitors		12S Celem CSM 150/300
Gen. 1 Encapsulant		Aremco 2315
Gen. 2 Encapsulant		Cooltherm SC-320

losses using the calculated fields of the coil geometry from the FAM. To include losses at the fundamental frequency and from the higher order, odd harmonic currents in the tank, the frequency-dependent resistance of the conductors and resonant capacitors were included. Overall, the coil current is highly sinusoidal and most of the loss comes from current at the fundamental frequency. At the 120 kW operating point, the fundamental current in the GA was measured as 167 A(rms), with third harmonic of 5 A(rms), and fifth harmonic of 1 A(rms), yielding a total harmonic distortion of approximately 3%. The modeled nonlinear ferrite hysteresis losses are normalized by square of the rms fundamental current resulting in an amplitude-dependent resistance as in Fig. 5. Likewise, the calculated ferrite flux density and ferrite hysteresis loss are shown in Fig. 6. In these plots, the outer ferrite thickness is 5 mm and the inner region is a thickness of 10 mm as in Table IV. The measured impedance of the Litz wire leads to the inverter and rectifier, as in Table IV, is also added to the resistance and inductance used in the simulations. The leads are shown as additional inductance in the overall circuit diagram with inductance of L_{lead} and resistance of R_{lead} in Fig. 7. Here, the temperature of the wire is set at 40 °C as predicted by thermal modeling and measurements described later.

PLECS is used to simulate the dynamic performance of the system and the performance of the inverter and rectifier. PLECS models device thermal effects on conduction and switching losses and deadtime intervals t_{dt} by including temperature-dependent conduction and switching loss models for devices with lookup tables or equations. The 1.2 kV SiC MOSFET half-bridge modules Wolfspeed/Cree CAS325M12HM2 and ROHM BSM300D12P2E001 are used in the inverter and rectifier, respectively. The rectifier uses the anti-parallel Schottky diodes of the ROHM modules to form a passive rectifier. The thermal capacitance of the devices in the PLECS model is reduced in order to achieve steady-state temperatures quickly.

Device switching losses are dependent on many factors, such as power loop inductance and gate driver specifications, voltage, layout, and gate resistance values, which affect the turn-OFF and turn-ON times of the devices, but datasheets often only provide switching losses for one set of tests under hard switching conditions. To extrapolate values from manufacturer data for use in modeling soft-switching losses, the turn-OFF loss in each period when soft-switching, $E_{\text{off,ss}}$, is then approximated from the datasheet hard-switching turn-OFF loss, E_{off}, by [26]

$$E_{\text{off,ss}} = E_{\text{off}} - E_{C\text{oss}}. \tag{21}$$

For the Cree/Wolfspeed CAS325M12HM2, the nominal C_{oss} value at 1000 V is used to derive the soft-switching turn-OFF loss table from the datasheet hard-switching turn-OFF loss in with a gate drive voltage of −5/+20 V. Greater accuracy would be obtained by accounting for the nonlinear C_{oss} capacitance [27]. In the tests, the Cree/Wolfspeed gate driver board CGD1700HB3P-HM3 was used, which generates a gate drive voltage V_{GS} of −4/+15 V. This causes a slight increase in the nominal on-state resistance to $R_{DS} = 4$ mΩ from the nominal value. For the switching loss, only −5/+20 V plots were given so these are used in the PLECS model.

D. Selection of Ferrite and Litz

The loss models are used to inform the the selection the Litz wire size and ferrite thickness as a tradeoff of loss and weight for the geometry output from the FAM optimization. Limiting the weight of the ferrite and Litz contributes to the goal of high gravimetric power density.

First, the ferrite thickness is swept for the Ferroxcube 3C95 and Epcos N95 material using the ferrite loss model in Fig. 8(a). From these curves, a thickness of 10 mm of ferrite or around 9.8 kg with Ferroxcube 3C95 ferrite is chosen. Similar to the approach in [28], further lightweighting is achieved in the demonstrator design by reducing the ferrite to 5 mm thickness in the outer region of the ferrite sheet to reduce the weight to around 6.0 kg. This increases the ferrite loss per side from around 161–267 W. The inner region dimension is chosen by using a 6 × 2 grid of 50.8 mm × 64.0 mm ferrite tiles for an overall 30.7 cm × 13.0 cm area.

Next, the size of the Litz wire of the coil is chosen. In Fig. 8(b), the result the sweep of Litz wire size is plotted in terms of weight

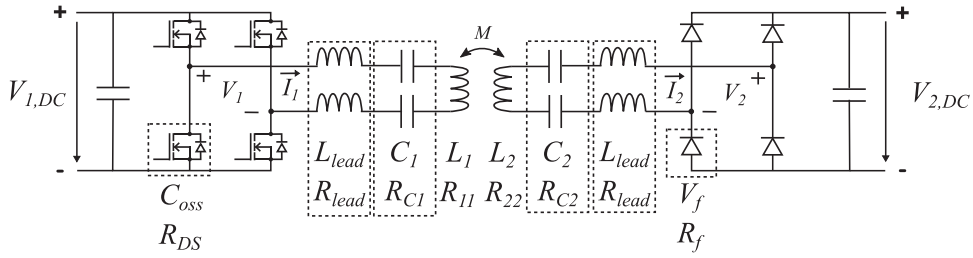

Fig. 7. Gen. 1 and Gen. 2 circuit schematic labeled with component parameters. Both demonstrator systems consist of matched, series-series compensated coils driven by a MOSFET full-bridge inverter with a diode rectifier.

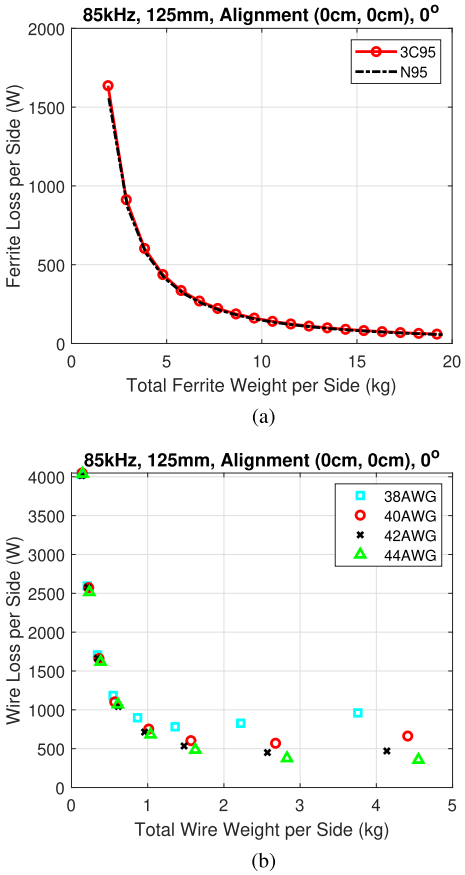

Fig. 8. Loss and weight of different (a) ferrite thicknesses and (b) Litz wire diameters and stranding. The overall cable size is swept from 16 to 2 AWG equivalents from left to right.

and loss. In this plot, the length of the wire is kept constant at 10.8 m, the length calculated from the contours of the coil geometry, and different gauges of wire are swept according to manufacturer standard Litz constructions from 16 to 2 AWG standard gauges of 38 to 44 AWG strands, resulting in points from left to right, respectively. Here, as the equivalent gauge of wire is increased more strands of wire are added in parallel which decreases the dc resistance. This would normally also lead to a decrease in the ac resistance. However, for this geometry, the proximity effect loss from these additional strands offsets

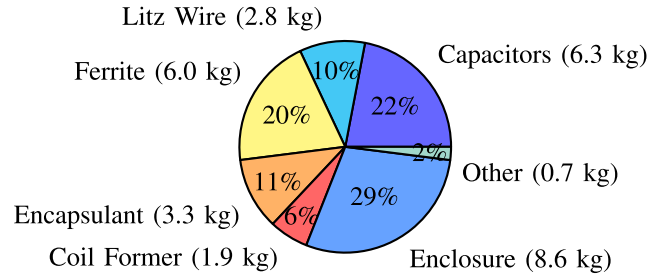

Fig. 9. Breakdown of the weight of one Gen. 2 demonstrator coil assembly.

and eventually overcomes the decrease in dc resistance in larger gauge of Litz wire, especially with the thicker 38 and 40 AWG stranding. This limits the benefit of the thicker equivalent gauges of wire from the loss and weight perspective. From this analysis, Litz wire with equivalent 4 gauge and 42 AWG stranding was chosen as the conductor for the demonstrators.

The physical implementations of the demonstrators are designed with this ferrite and Litz wire selection. A breakdown of the weight of the final demonstrator is shown in Fig. 9. As later discussed, two generations of the demonstrator were built: a Gen. 1 and Gen. 2. Both versions are very similar in physical construction and weight. Overall, the demonstrators are comprised of a polycarbonate cover and coil former, a Litz wire coil, a layer of ferrite, an aluminum enclosure, copper tubing, and the capacitor banks. The overall assembly weight including the compensation capacitor banks was 29.3 kg in a 42.0 cm $\times$ 54.0 cm coil area. An overview of these parts can be seen in Fig. 10. Here, the ferrite, Litz wire, and encapsulant are 41% of the weight of the assembly, respectively, while the capacitor banks comprise 22% of the weight. As seen, the weight of the unmodeled components, such as the enclosure, coil former, compression plates, and resonant capacitor banks, are large compared to the modeled weights of the ferrite and wire. Many opportunities for weight reductions exist in future work. In particular, the enclosure, coil former, capacitor compression plates, and other structural parts could be redesigned to be made thinner or with lighter materials to reduce their weight. Other magnetic materials, such as nanocrystalline ribbon cores [29], could also be considered to further reduce the thickness and weight of the demonstrators in future work.

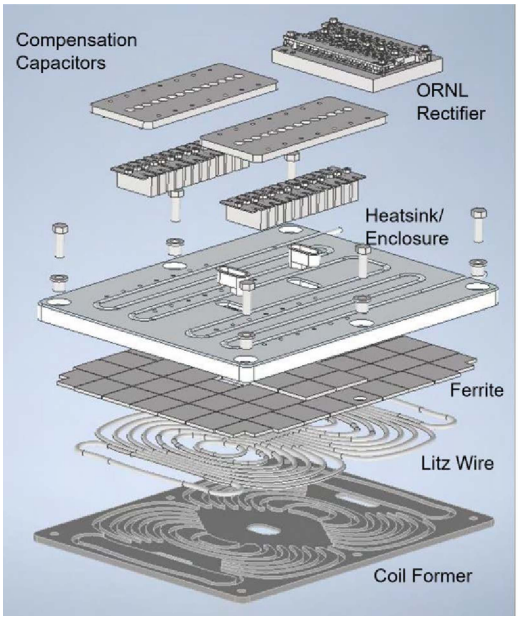

Fig. 10. Exploded view of the different layers of the demonstrator coil assembly. Here, the assembly consists (bottom to top) of a polycarbonate cover and coil former, a Litz wire coil, a layer of ferrite, an aluminum enclosure, copper tubing, and the capacitor banks. A sample rectifier designed by ORNL is shown as well for optional mounting in a single-box solution. In the benchtop testing, the rectifier was placed on a separate table for ease of access.

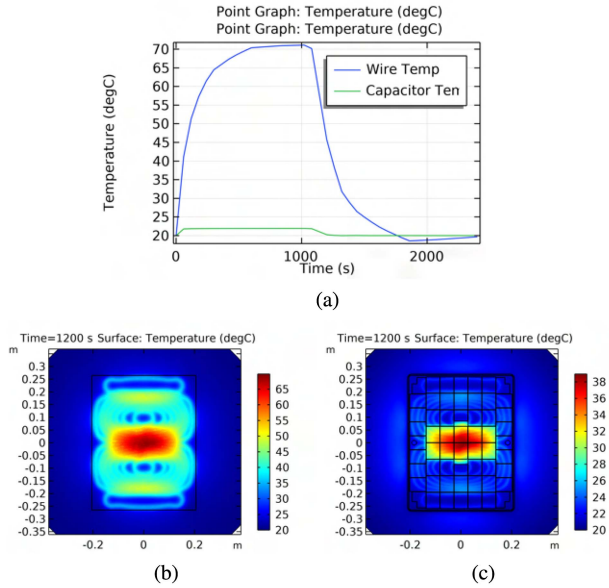

Fig. 11. Thermal FEA simulations of the Gen. 2 120 kW coil assembly at maximum misalignment with the modeled worst-case losses at 120 kW with 20 min of operation: 1200 W of wire loss, 600 W of capacitor loss, and 800 W of ferrite loss. (a) Temperature over time of the center of the wire and one of the backside capacitors. (b) Temperature distribution on the surface of the wire. (c) Temperature distribution 2.5 mm from the surface of the ferrite.

E. Thermal Modeling and Design

The demonstrators have indirect liquid cooling to limit the temperature rise of the components and increase operating time similar to the approach of [10]. To motivate the need for liquid cooling in the 120 kW demonstrators, an FEA thermal simulation of the demonstrator was performed.

Using the interface of the heatsink and the ferrite as a constant temperature boundary condition, FEA simulations of the coil assembly were performed to model the thermal performance of the design as in Fig. 11. These simulations use a constant temperature boundary in the channels to model the effect of the copper tubing. The worst-case losses in the coil were modeled at the nominal power level of 120 kW with each modeled loss evenly distributed throughout the volumes of the Litz wire, ferrite, and capacitors, respectively. The FEA-derived thermal performance of the 120 kW demonstrator design predicts steady-state operation at 120 kW with a wire temperature rise of 55 ^{o}C relative to the channel surfaces with backside cooling. The temperature rise in the center of the coil is 0.0275 K/W with the 1200 W of wire loss and 800 W of ferrite loss used in the model.

III. Experimental Validation of the Gen. 1 Demonstrator

A. Gen. 1 Demonstrator Construction

The Gen. 1 of the demonstrator was constructed using Aremco 2315 epoxy as the encapsulant on both the back and front sides of the enclosure. Aremco 2315 was initially chosen as it is mechanically and thermally robust with good adhesion and thermal conductivity. Each cure of this black-colored epoxy required a cure time of 6 h at 120°C such that a large oven was needed to cure the entire coil assembly in multiple steps. In each use of the Aremco 2315 epoxy, the resin and hardener parts were mixed and then degassed in a vacuum chamber to eliminate air bubbles. Several images of the process are shown in Fig. 12 including the setting of the copper tubing, layout of the ferrite, and encapsulation of the tubing, coil and ferrite. In Fig. 12(a), the end result of the tubing preparatory work is shown. The tubing was bent with a hand tool to shape; pressed into the channels with strips and sheets of wood, clamps, and weights; and set with room-temperature epoxy. The layout of the ferrite tiles in the Gen. 1 coils is shown in Fig. 12(b). The layout differs slightly from the planned arrangement due to the slight difference in tile width used in the computer-aided design (CAD) and simulations compared to the actual tile width. This led to the rotation of some tiles and the addition of some cut pieces as spacers. Likewise, layout and numbering of the ferrite was done to match tolerances between tiles and ensure all pieces would fit before applying encapsulant.

B. Capacitor Bank Construction

The demonstrator coil assemblies include compensation capacitors mounted to the backside of each enclosure. In total, 12 compensation capacitors, the 1 μF Celem CSM 150/300 conduction cooled capacitors with maximum ratings of 700 V(rms) and 450 A(rms) are connected to the coil in series and divided into two banks of six capacitors each. Copper bus bars connect the capacitors with torqued bolts, washers, and nuts as in Fig. 13(a). Cooling of the capacitors is accomplished by thermal contact

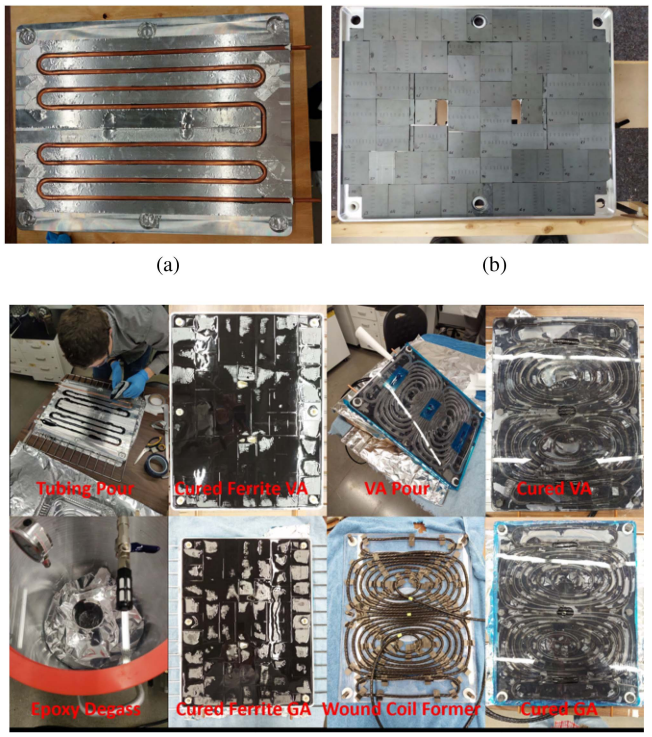

(a) (b) (c)

Fig. 12. Construction of the Gen. 1 120 kW coil assemblies. (a) Bent tubing pressed and bonded into the channels in the aluminum enclosure. (b) Ferrite layout and numbering of the Gen. 1 coil assembly with a similar layout used in the other coil. (c) Multiple images of tubing, ferrite and coil encapsulation, degassing of the epoxy, wound coil former, and front sides of the finished Gen. 1 coils.

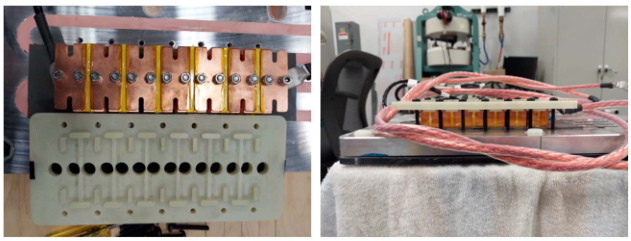

(a) (b)

Fig. 13. Compensation capacitor bank used in the demonstrators. (a) View of the disassembled compression plate, bus bars, and capacitors. (b) Side view of the assembled capacitor bank mounted on the Gen. 1 coil assembly.

with the cooled aluminum enclosure through large, insulating thermal pads with clamping force supplied by the compression plates. The compression plates in Fig. 13(b) are made of G10 composite material and align the capacitors and busbars that fit in the raised notches on the plates. The compression plates are attached and screwed into threaded holes in the aluminum to provide adequate clamping force for thermal contact. The nuts on top of the busbars fit into holes in the plates, which prevents creepage paths between the corners of the nuts. A layer of mylar tape on the bottom of the capacitors and between the nuts at the top of the busbars provides additional insulation.

This compensation capacitor bank design has several benefits. Conductive cooling of each capacitor is accomplished while keeping the busbars and fasteners away from the aluminum enclosure. The alignment of the capacitors and busbars in series arrangement, which is normally difficult due to the single-bolt package of the capacitors, is resolved by the notches in the compression plate. Finally, the capacitors are mounted close to the wire passthroughs, reducing the need for extra wire for leads or additional heatsink weight in the system.

C. Testing of the Gen. 1 Demonstrator

Extensive measurements of the Gen. 1 demonstrator were taken including impedance, mutual inductance, efficiency, thermal performance, and stray field measurements. The efficiency and stray field measurements are described here, while the impedance measurements are summarized later in Section IV-B1 in direct comparison to the Gen. 2 impedance measurements. The Gen. 1 efficiency measurements used the 1X Inverter and test setup of Fig. 22 as later described in detail in Section IV-B2.

1) Gen. 1 Efficiency and Thermal Measurements: The Gen. 1 GA and VA were tested up to 90 kW output power over a variety of loading conditions and misalignments. For the aligned[1] condition with near-unity gain with constant output resistance, the test results are plotted in Fig. 14. In Fig. 14(a), the inverter, coil–coil, and rectifier efficiencies are shown alongside the dc/dc efficiency. In these measurements, phase compensation of the high-frequency current probes was not performed, which led to some inaccuracy of the power factor and ac power and efficiency breakdown. However, the measured inverter, coil–coil, and rectifier efficiencies are still informative, as they clearly show the decrease in coil–coil efficiency as the power level increases and lower rectifier efficiency associated with the rectifier forward voltage drop.

At low power levels, the coil–coil efficiency is high, matching the low-amplitude measurements of resistance and impedance of the Gen. 1 GA and VA. At high power levels, the coil–coil efficiency plot has perturbations in efficiency. This is due to pulsed measurements and the effect of temperature on the coil efficiency. Measurements after some resting time led to slightly higher efficiencies as seen in the perturbations in coil–coil efficiency at high-power levels. A summary of the Gen. 1 dc/dc efficiency measured at other alignments is given in Table V at the highest power levels achieved compared to the modeled values. As seen, the measured dc/dc efficiency is much lower than modeled as a result of the rapid dropoff in coil–coil efficiency.

A 3-min duration test at 60 kW was performed to assess system temperatures. For this test, the coils were cooled with a VWR 1175MD chiller with glycol-water coolant at a pressure of 62 kPa, coolant flow rate of of 1 L/min, and set point of 19 °C, with the GA and VA coolant tubes in series. The test data is shown in Fig. 14(b). Some cracking noises that may

[1] After analyzing the measurement data, it later was measured that the alignment grid lines used to align the VA was off by around -7 mm in the X-direction and 5 mm in the Y-direction such that the actual test alignment was off in those directions. All misalignment numbers are given with this offset for the rest of this paper for measurements of both the Gen. 1 and Gen. 2 demonstrators.

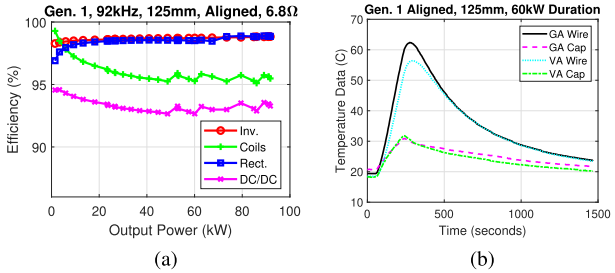

(a) (b)

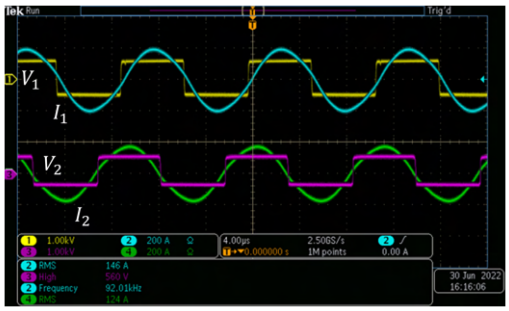

(c)

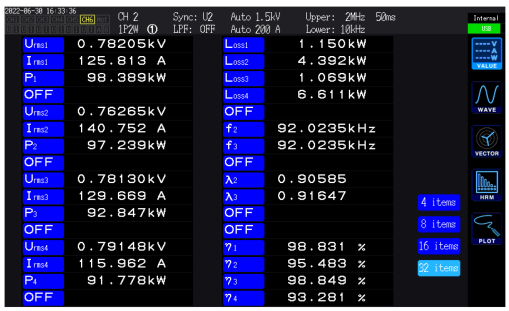

(d)

Fig. 14. Test results of the Gen. 1 demonstrator at alignment and 125 mm. (a) Efficiency breakdown up to 91.8 kW output power. (b) Thermal measurements of the system during testing points around 91.8 kW. (c) Waveforms at 91.8 kW output. (d) Power analyzer screenshot at 91.8 kW.

TABLE V
SUMMARY OF THE MEASURED AND MODELED DC/DC EFFICIENCY OF THE GEN. 1 DEMONSTRATOR AT DIFFERENT ALIGNMENTS AT 125 MM AIRGAP

Alignment (X,Y)	DC Output Resistance	Power Level	Meas. DC/DC Eff.	Model DC/DC Eff.
(0 cm, 0 cm)	6.8 Ω	91.8 kW	93.3%	96.3%
(5 cm, 0 cm)	5.9 Ω	48.5 kW	93.3%	96.2%
(10 cm, 0 cm)	5.5 Ω	46.7 kW	91.8%	95.3%
(0 cm, 5 cm)	5.5 Ω	44.2 kW	92.1%	95.2%

have been caused by thermal expansion were heard during the testing. As seen, the temperatures of the GA and VA coils rapidly rise from 20 °C to around 62.4 °C and 56.4 °C, respectively. The temperatures of the GA and VA capacitors stay lower with temperatures reaching a maximum of around 30 °C. Due to the low coolant flow rate, the temperatures take around 21 min to return to close to the starting temperatures. These thermal data support that much of the loss is in the GA and VA assemblies as in the efficiency measurements. The continued increase in

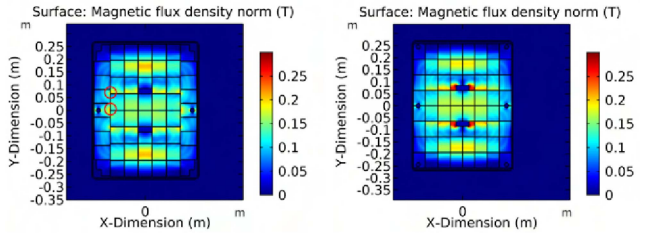

(a) (b)

Fig. 15. FEA simulations of ferrite layouts for the (a) Gen. 1 coil assemblies with two "T" intersections labeled with red circles and the (b) Gen. 2 coil assemblies. Both flux density plots are taken at 2.5 mm from the surface of the ferrite at the peak flux of the nominal 164 A(rms) coil current.

temperature after the end of the 3-min period at 60 kW also suggests that the ferrite beneath the wire may be hotter than the wire itself and possibly the source of much of the loss.

2) Gen. 1 Stray Field Measurements: To assess the stray field performance of the Gen. 1 demonstrator, the fields of the system were measured at a distance of 80 cm away from the center of the airgap with a NARDA EHP-200 A field probe as in Table VI. As shown, the fields increase on both axes under misaligned conditions, but more significantly on the axis in the direction of offset. The stray field is comprised of fields in the X, Y, and Z directions. These B_x, B_y, and B_z components may not be in phase, the vector sum of the three is often used as the total worst-case magnetic field used to compare with the reference values in the standards [6].

D. Circulating Flux, Flux Concentrations, and Residual Stress

Following the low efficiency measured on the Gen. 1 demonstrator, an investigation was performed to determine the cause of the unexpected losses seen at higher power levels. The stray field performance, mutual inductance, and impedance of the system matched model predictions, but the efficiency did not. The lower efficiency was also seen in the thermal performance of the system, limiting the power level and duration of the testing. The result of this investigation was changes to the ferrite tile layout, the routing of the wire passthroughs to the backside of the coil assemblies, and the type of thermally conductive encapsulant in a Gen. 2 demonstrator.

The use of discrete ferrite tiles in the 120 kW demonstrators places many small air gaps within the ferrite sheet. Depending on the location of these gaps, localized concentrations of flux may occur possibly causing hot spots within the ferrite. As detailed in [30], several locations for flux concentrations were found in the Gen. 1 ferrite layout making it necessary to modify the layout in the Gen. 2 layout to allow a consistent ferrite pattern with more ideal "cross" intersections. Comparison of the two ferrite patterns is shown in Fig. 15. Here, flux concentrations around "T" intersections are seen in the Gen. 1 layout and are reduced in the simplified Gen. 2 layout. The Gen. 2 layout produces higher flux density in the tiles close to the passthroughs due to inner corners cut into the ferrite to accommodate the openings. Smaller tiles are also used in the Gen. 2 simulation to match the part dimensions.

TABLE VI
MEASURED RMS STRAY FIELD (B_x, B_y, B_z) OF THE GEN. 1 DEMONSTRATOR AT 80 CM AT AN AIRGAP OF 125 MM

Alignment (X,Y)	Measurement Output Power	X-axis (Scaled to 120 kW)	X-axis Vector Sum (Scaled to 120 kW)	Y-axis (Scaled to 120 kW)	Y-axis Vector Sum (Scaled to 120 kW)
(0 cm, 0 cm)	50.0 kW	3.81 μT, 2.11 μT, 1.07 μT (5.90 μT, 3.27 μT, 1.66 μT)	4.48 μT (6.95 μT)	1.87 μT, 2.17 μT, 1.74 μT (2.90 μT, 3.36 μT, 2.70 μT)	3.35 μT (5.19 μT)
(5 cm, 0 cm)	48.4 kW	4.32 μT, 2.73 μT, 1.23 μT (6.80 μT, 4.30 μT, 1.94 μT)	5.26 μT (8.28 μT)	1.92 μT, 2.07 μT, 1.77 μT (3.02 μT, 3.26 μT, 2.79 μT)	3.33 μT (5.25 μT)
(10 cm, 0 cm)	46.7 kW	5.93 μT, 4.12 μT, 1.60 μT (9.51 μT, 6.60 μT, 2.56 μT)	7.40 μT (11.86 μT)	2.29 μT, 2.39 μT, 2.06 μT (3.67 μT, 3.83 μT, 3.30 μT)	3.90 μT (6.25 μT)
(0 cm, 5 cm)	44.2 kW	3.77 μT, 2.35 μT, 1.15 μT (6.21 μT, 3.87 μT, 1.89 μT)	4.59 μT (7.56 μT)	2.05 μT, 2.29 μT, 2.11 μT (3.38 μT, 3.77 μT, 3.48 μT)	3.73 μT (6.14 μT)

Misalignment toward probes.

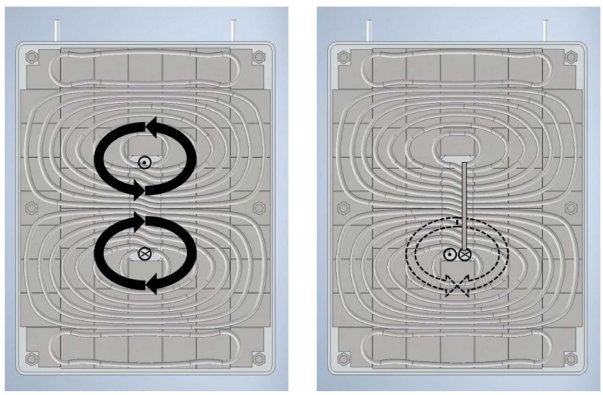

Fig. 16. (a) Formation of circulating flux in the Gen. 1 ferrite sheet from two separate lead currents entering and leaving through separate passthroughs. (b) Elimination of circulating flux using a single passthrough.

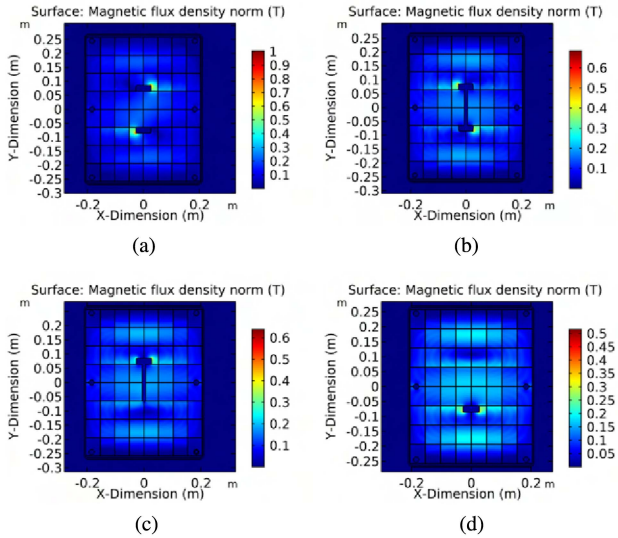

Fig. 17. FEA simulation outputs of the flux density 2.5 mm from the surface of the ferrite with different options to reduce the circulating flux. (a) Baseline case with two openings and separate wire passthroughs. (b) Two openings with a 1.3 cm width center notch in the ferrite and separate wire passthroughs. (c) One opening with a 1.3 cm width center notch in the ferrite. (d) Best case with one opening and no notches.

In both the Gen. 1 and Gen. 2 demonstrators, Litz wire passes through the aluminum enclosure and ferrite from the frontside to the backside of the enclosure where the compensation capacitors are mounted. Routing the wire in this manner reduces the need for additional coil area outside the ferrite to route the wires and minimizes the high-frequency conductor length. However, this requires a gap in the ferrite sheet, which may lead to flux concentrations and higher overall ferrite loss than in an unbroken ferrite layer of the same thickness. As discussed in [30], passing the leads through separate holes can result in circulating flux and additional losses. This loss, as with most other ferrite losses, is nonlinear and minimally present in low-amplitude measurements, such as coil or tank resistance measurements, with an impedance analyzer.

Circulating flux can be avoided by making the total passthrough current equal to zero. This is best accomplished by having both the incoming and outgoing wires pass through the ferrite sheet together such that their currents cancel. In the Gen. 1 coils, two separate passthroughs produced circulating flux around each opening. When this occurs, the circulating current is additive between the openings as in Fig. 16. In the Gen. 2 demonstrator, the Litz wire is rerouted to return through a single passthrough. The FEA simulation outputs in Fig. 17 estimate the impact of the circulating current on the ferrite loss in different options for rerouting the Litz wire or notching the ferrite. Two main options are explored: making a notch in the center ferrite between the Gen. 1 openings to pass the wire underneath the coil to a single passthrough and passing the wire over the coil to a single passthrough by extending a hole in the coil former. Each case is simulated at the peak flux from the nominal coil current of 164 A(rms) and a volume integral of the flux density to the $\beta = 2.44$ term of the 3C95 ferrite to determine the relative impact on the ferrite loss compared to the base case as in Table VII. As shown, the use of a notch to eliminate the main circulating flux path is effective, but does slightly increase the loss relative to the best case with an unbroken sheet of ferrite with the return wire routed over the center conductors, as in the Gen. 2 coil assembly.

Finally, as detailed in [30], the large compressive stress caused by the Aremco 2315 epoxy in the Gen. 1 demonstrator resulted in some of the additional losses. Large compressive stress has been shown to decrease the magnetic performance of MnZn ferrite [31]. As discussed, the Gen. 1 coil assemblies were cured at 120 °C and then cooled to room temperature. Differences

TABLE VII
COMPARISON OF FERRITE LOSS FROM FEA SIMULATIONS OF THE DIFFERENT PASSTHROUGH OPTIONS OF FIG. 17 WITH THE GEN. 2 FERRITE LAYOUT AND COIL CURRENT OF 164 A(RMS)

Simulation	Peak $B^{2.44}$ Volume Integral	Relative Loss
Baseline Two Openings	10.4e-6	-
Two Openings with Center Notch	7.0e-6	−32.7%
One Opening with Center Notch	6.6e-6	−36.5%
One Opening with Passover Routing	6.4e-6	−38.5%

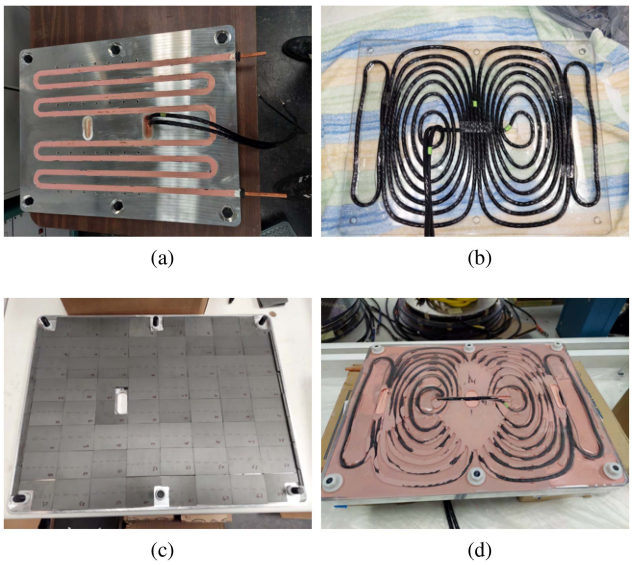

Fig. 18. Construction of the Gen. 2 120 kW coil assemblies. (a) Bent tubing pressed and bonded into the channels in the aluminum enclosure and covered with encapsulant. (b) Coil former with routed wire taped in place. (c) Ferrite layout and numbering of one of the Gen. 2 coil assemblies. (d) Frontside of a cured Gen. 2 coil.

in the thermal expansion coefficients of the ferrite, epoxy, and aluminum alongside the high hardness and Young's moduli of the materials result in large compressive stress [32]. In the Gen. 2 coil assemblies, this stress is significantly reduced by using a softer, room-temperature curing silicone elastomer as the encapsulant.

IV. EXPERIMENTAL VALIDATION OF THE GEN. 2 DEMONSTRATOR

A. Construction of the Gen. 2 Demonstrator

Images of the Gen. 2 assembly process are shown in Fig. 18. The Gen. 2 coils were constructed using Lord Coolthern SC-320 as the encapsulant. SC-320 is a pink-colored silicone elastomer that can be cured at room temperature for 24 h. The design and construction of the Gen. 2 coil assemblies was similar to that of the Gen. 1 assemblies, but with improvements. In the Gen. 2 aluminum enclosures, the tubing channels were widened by 3.2 mm to make fitting the tubing easier. The inner section

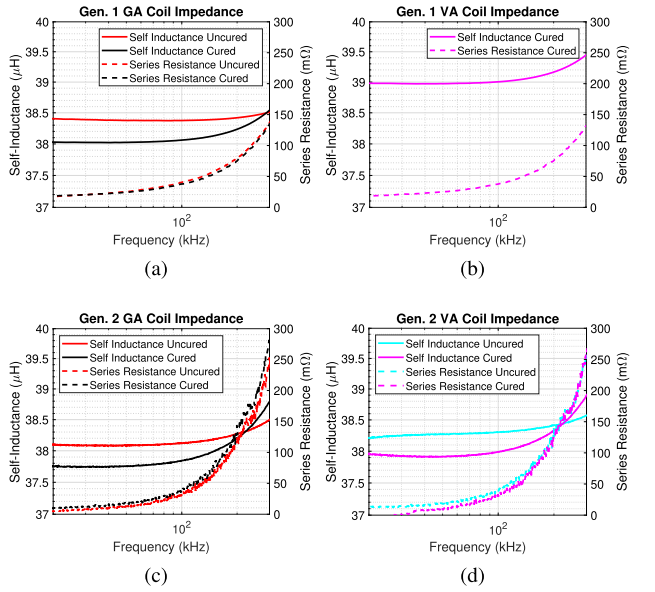

Fig. 19. Measured self-inductance and series resistance of the uncured and cured coils without the presence of the other coil. (a) Cured and uncured measurements of the Gen. 1 GA coil. (b) Cured measurements of the Gen. 1 VA coil. In this case, measurements were only taken after assembly and were not captured before curing. (c) Measurements of the uncured and cured Gen. 2 GA coil. (d) Measurements of the uncured and cured Gen. 2 VA coil.

of the cavity was widened to simplify the overall ferrite layout. One passthrough was also eliminated so that both wires were routed together through one opening. The cutting of the ferrite tiles in Fig. 18(c) was accomplished more cleanly than in the Gen. 1 assemblies by the use of a wet tile saw with a continuous diamond blade. This method made precise cuts to the ferrite and prevented the ferrite from shattering from thermal shock as when cutting with a rotary tool in the Gen. 1 construction.

B. Testing of the Gen. 2 Demonstrator

Measurements of the impedance, mutual inductance over misalignment, waveforms, stray fields, and efficiencies of the Gen. 2 demonstrator were taken to compare with modeled values and the measurements of the Gen. 1 demonstrator.

Images of the overall of the test setup, inverters, and rectifier are given in Fig. 22. A Hioki PW6001 power analyzer was used to capture the voltage, current, and losses. To measure coil currents, the Hioki CT6904 A current sensor was used with datasheet phase compensation. During some of the tests, this allowed the losses of each stage to be measured with accurate higher frequency ac power measurements at the output of the inverter and input of the rectifier. Most test points in the efficiency sweeps were attained for short durations such that the temperatures in the GA and VA remained low and thermal effects were not dominant. During the tests, the four-channel Omega FOB100 fiber optic thermometer was used. This type of temperature probe is not affected by magnetic fields, so temperature measurements were taken during operation. Temperatures were typically measured on the GA and VA on the surfaces of

TABLE VIII
MEASURED VERSUS MODELED GEN. 1 AND GEN. 2 SELF-INDUCTANCE AND RESISTANCE ALIGNED AT 125 MM AIRGAP FROM *LCR* METER AT 85 KHZ

	Self-Inductance (L_1, L_2)		Series Resistance (R_{11}, R_{22})		
	Measured (GA, VA)	Modeled (Coil Only 10.2 m)	Measured (GA, VA)	Modeled (Coil Only 10.2 m)	Modeled (With Leads 11.9 m)
Gen. 1	37.9 μH, 38.1 μH	37.4 μH	35 mΩ, 36 mΩ	19.7 mΩ	23 mΩ
Gen. 2	38.9 μH, 39.1 μH	37.4 μH	23 mΩ, 16 mΩ	19.7 mΩ	23 mΩ

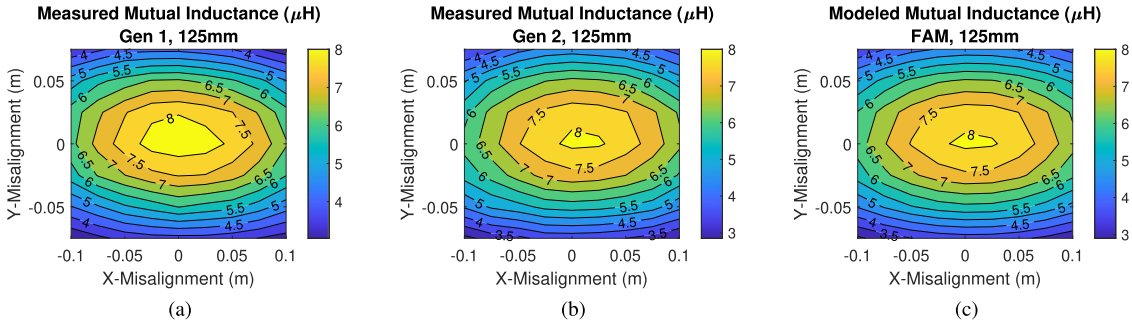

Fig. 20. Measured mutual inductance of the Gen. 1 and Gen. 2 coils compared to the modeled values. (a) Measured mutual inductance of the Gen. 1 coils. (b) Measured mutual inductance of the Gen. 2 coils. (c) Modeled mutual inductance from the FAM.

the resonant capacitors and at the center of the coil geometry on the surface of the outer insulation of the Litz wire cable.

1) Impedance and Mutual Inductance Measurements: Impedance measurements of the Gen. 1 and Gen. 2 coil assemblies were taken using *LCR* meters and impedance analyzers. To assess the effects of curing on the coils, measurements were taken before and after curing the coils with encapsulant. The self-inductance and resistances of the Gen. 1 and Gen. 2 coils with respect to frequency are shown in Fig. 19. Different impedance analyzers, the Aligent E4990 A and the Omicron Lab Bode 100, were used in the measurements of the Gen. 1 and Gen. 2 systems, respectively. The modeled values for self-inductance and resistance are compared with the values measured by *LCR* meter in Table VIII. For the resistance modeling, the total length of wire including the wire outside the coil geometry used as leads to the capacitor banks were included totalling 11.9 m. Measurements were taken with the coils aligned at an air gap of 125 mm as the presence of ferrite across the airgap slightly increases the self-inductance values. The mutual inductance of the coils was found by measuring the inductance of the series combination of the coils over different misalignments and subtracting the measured self-inductance of the coils. Mutual inductance measurements compared to the FAM modeled values are shown in Fig. 20.

In both demonstrators, two capacitor banks with a series combination of 12 1 μF Celem CSM150/300 capacitors were used to form a series tank with the GA and VA coils. The capacitance and series resistance of one of these capacitor banks are given in Fig. 21(a) and compared to the modeled values in Table IX. As seen, the capacitors are affected by a parasitic resonance such that the capacitance increases with frequency, especially above 100 kHz. The two Gen. 2 tank impedances are also shown in Fig. 21(c) and (d), with some parasitic resonances seen in the MHz range. There is a difference in the series resistance measurements with the *LCR* meter in Table IX and the Bode 100 impedance analyzer measurements in Fig. 21(a) possibly due to differences in the setup, calibration, or tolerances of the two instruments. The measured inductance and series resistance of the leads are also plotted in Fig. 21(b) as included in the loss models.

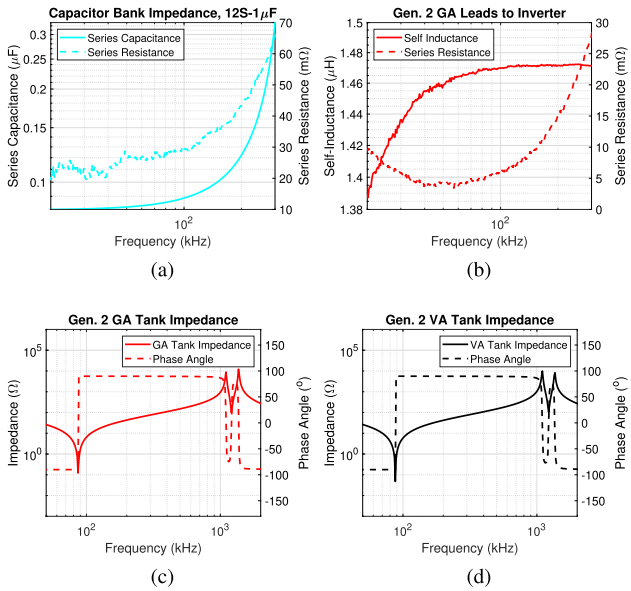

Fig. 21. Measurements of the tank elements comprised of 12 1 μF Celem CSM 150/300 capacitors and series tank impedance with the Gen. 2 coils. (a) Measured capacitor bank series capacitance and resistance. (b) Measured lead impedance to and from the GA and VA to the inverter and rectifier. (c) Cured measurements of the Gen. 2 GA tank. (d) Cured measurements of the Gen. 2 VA tank.

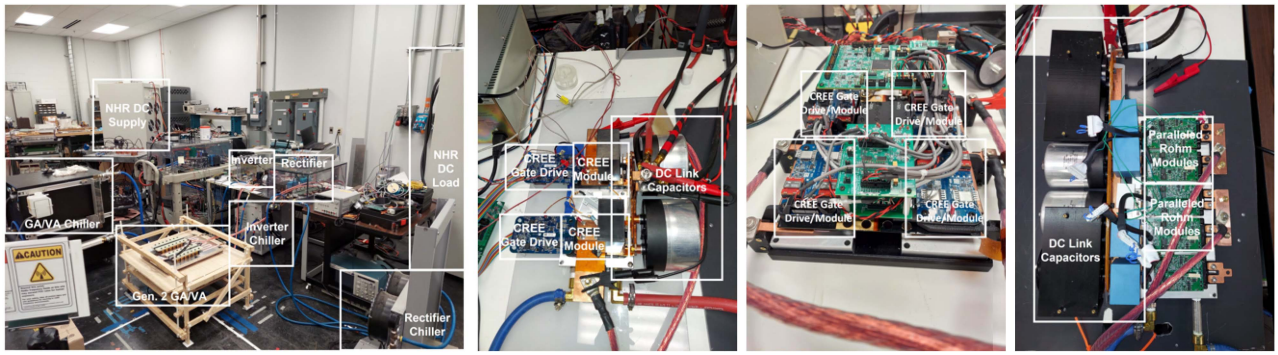

Fig. 22. Images of the Gen. 1 and Gen. 2 test setup. (a) Overall test setup including 100 kW DC sources on the input and output of the system, chillers, and airgap holder. (b) ORNL 120 kW full bridge 1X Inverter [11], (c) ORNL full bridge 2X Inverter with four half-bridge modules [33], and (d) ORNL ROHM module converter used as the test rectifier.

TABLE IX
MEASURED VERSUS MODELED CAPACITOR BANK IMPEDANCE AT 85 KHZ BY *LCR* METER (CELEM CSM 150/300)

	Series Capacitance (C_1, C_2)		Series Resistance (R_{C1}, R_{C2})	
	Measured (GA, VA)	Nominal	Measured (GA, VA)	Modeled
12S-1 μF Bank	84.1 nF, 84.1 nF	83.3 nF	9 mΩ, 10 mΩ	9.6 mΩ

Some of the difference in series resistance and self-inductance of the Gen. 1 and Gen. 2 coils may come from the additional 1.8 m of coil wire length of the Gen. 1 coils compared to that of the Gen. 2 coils when the measurements were taken, resulting in higher resistance for the Gen. 1 coils. The lower self-inductance of the Gen. 1 assemblies may be caused by decreased ferrite permeability due to the mechanical stress caused by the ferrite as detailed in [30]. However, the impedance measurements of the Gen. 1 and Gen. 2 demonstrators are similar and most of the effects that cause the difference in efficiency are not seen in low-amplitude impedance measurements. Although there were significant differences in the implementation of the two generations of demonstrators and measured efficiency, the fields and impedance of the Gen. 1 and Gen. 2 demonstrators are not largely different as they use the same geometry derived from the FAM optimization.

2) Gen. 2 Efficiency and Thermal Measurements: The performance of the Gen. 2 coils was tested at an airgap of 125 mm over different alignments at operating points with close to unity gain, and with fixed 400, 600, and 800 V output voltages to explore operating points with mismatched loading and current. Inverters and rectifiers developed by Oak Ridge National Laboratory (ORNL) are used in the tests. The inverter from [11] was used as in Fig. 22(b) for the first set of tests while the second inverter in Fig. 22(c) from [33] with two parallel modules per half-bridge was used for later tests to slightly improve efficiency and to survive tests with higher current and longer duration.

The Gen. 2 demonstrator was tested up to 120 kW in various alignments with the 1X Inverter. Equipment similar to that in the

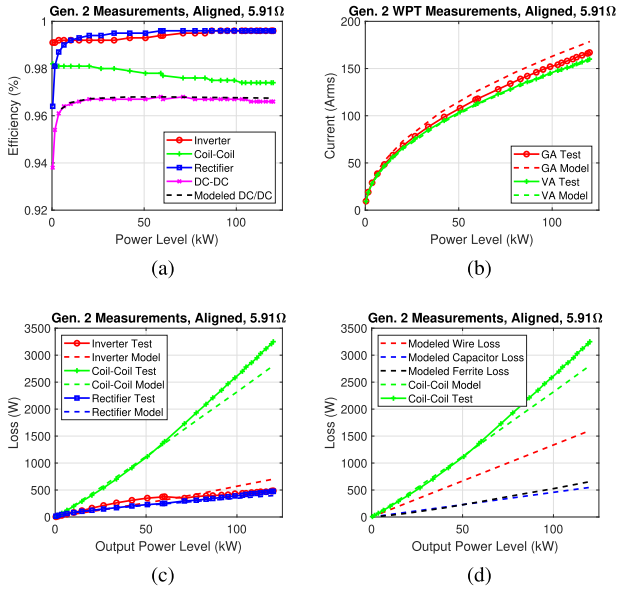

Fig. 23. Testing of the Gen. 2 demonstrator at alignment and 125 mm with the 1X Inverter. (a) Efficiency breakdown versus output power. (b) Measured versus modeled GA and VA current. (c) Measured versus modeled system losses. (d) Breakdown of the modeled coil–coil losses versus measured.

Gen. 1 tests was used to measure efficiency and temperatures. For the aligned condition up to 120 kW, the system efficiencies are shown in Fig. 23. The measurements are compared to the modeled efficiency as derived in PLECS using the parameters in Table IV. In the PLECS simulation, the modeled inductances were used, leading to a small error in the calculation of current and gain as in Fig. 23(b). For this test sweep, the Hioki PW6001 power analyzer and current probes were set up with phase compensation so that the breakdown between the inverter, coil–coil, and rectifier efficiency is more accurate than in the Gen. 1 tests. As seen, both the inverter and rectifier efficiencies increase with power level to peaks around 99.6% at 120 kW. Meanwhile, the coil–coil efficiency starts around 98.2% at low power and steadily decreases to 97.4% at 120 kW. The effect of the ferrite loss can be clearly seen in the increased coil–coil loss at

TABLE X
SUMMARY OF THE DC/DC EFFICIENCY OF THE GEN. 2 DEMONSTRATOR WITH THE 1X INVERTER NEAR UNITY GAIN AT DIFFERENT ALIGNMENTS AT AN AIRGAP OF 125 MM

Alignment (X,Y)	DC Load	Power Level	Meas. DC/DC Eff.	Model DC/DC Eff.
(0 cm, 0 cm)	5.9 Ω	120.4 kW	96.6%	96.7%
(5 cm, 0 cm)	5.9 Ω	64.2 kW	96.6%	96.8%
(10 cm, 0 cm)	5.9 Ω	52.7 kW	95.9%	96.0%
(0 cm, 5 cm)	5.0 Ω	51.2 kW	96.1%	96.2%
(10 cm, 5 cm)	4.1 Ω	51.7 kW	95.2%	95.1%

higher current and output power. The comparison of the overall modeled and measured coil–coil loss in Fig. 23(d) suggests that the ferrite losses may still increase faster at high power levels than modeled. This series of tests were pulsed measurements such that the temperatures of the GA and VA did not rise very much and thermal effects are small. The efficiencies near unity gain measured at other misalignments are summarized in Table X.

The Gen. 2 demonstrator was also tested and modeled with fixed output voltage loads to evaluate the performance of the system when connected to a battery. These conditions often result in mismatched GA and VA currents and nonunity gain operation, which results in lower coil–coil efficiency. In addition, when the equivalent output resistance decreases below the bifurcation limit, the input impedance of the system will become capacitive, leading to inverter hard-switching during device turn-ON. For the series–series compensated Gen. 2 demonstrator, this condition occurs when [16], [34]

$$k > \frac{R_L}{\omega_s L_2} \tag{22}$$

which is where $R_L < \omega_s M$ and below unity gain for matched GA and VA where $L_1 = L_2$. In a fast-charging application, this may occur at ideal alignment and low airgaps when high power is requested at low SoC and battery voltages.

The measured and modeled performance of the Gen. 2 demonstrator at an airgap of 125 mm with fixed output voltages of 400, 600, and 800 V are plotted in Fig. 24. To represent hard switching in the models, the inverter devices in the PLECS simulation were switched from soft-switching to hard-switching device models to calculate the switching losses. The efficiency decreases from hard-switching are clearly seen in the plots beyond the peak efficiency of each respective curve. For this series of tests, the upgraded 2X Inverter of Fig. 22(c) was used to increase the current capacity of the inverter for long-duration testing. This inverter has two Cree modules per half bridge instead of one, which decreases the conduction loss, and reduced loop inductance. With the upgraded inverter, the peak efficiency of the system increased to 97.3% from 96.7%. These tests were limited to 100 kW with one source and load dc supply and only up to near unity gain to preserve soft-switching operation. Here, the simulation model slightly overestimated the amount of GA current, possibly due to the additional commutation time of

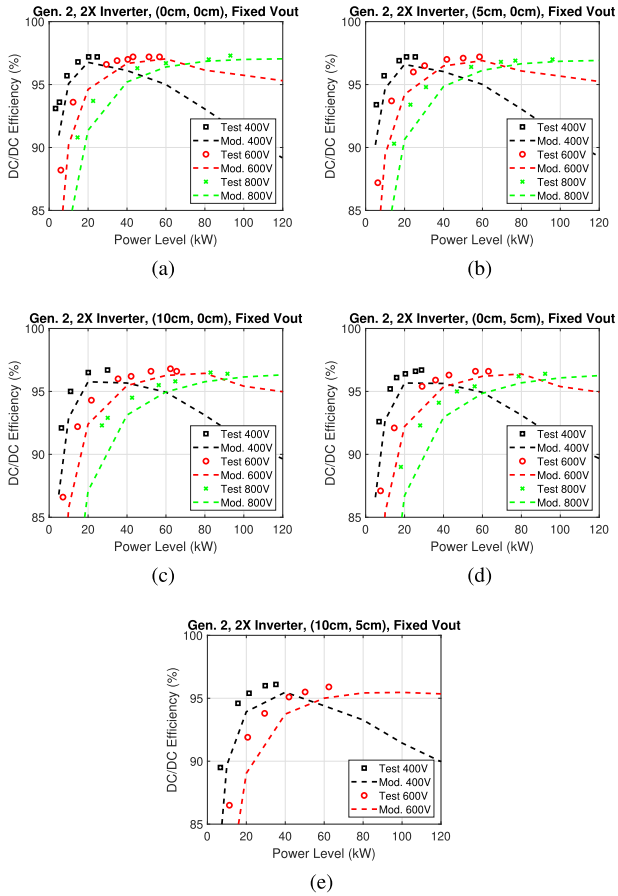

Fig. 24. Tests of the Gen. 2 demonstrator with the 2X Inverter at different alignments compared to modeled values at fixed output voltages and an airgap of 125 mm. DC/DC efficiency versus output power at (a) (0 cm, 0 cm), (b) (5 cm, 0 cm), (c) (10 cm, 0 cm), (d) (0 cm, 5 cm), and (e) (10 cm, 5 cm).

the 2X Inverter, resulting in a slightly lower modeled efficiency versus measured.

With the upgraded 2X Inverter, a 20 min, 50 kW output power test was performed at alignment at 125 mm airgap to assess the steady state temperature and overall thermal performance of the system. Using a fiber-optic thermometer, the temperatures of the GA and VA are measured during the test. Likewise, the power analyzer was used to record the measurement data at 15 s intervals. During the tests a large chiller, the Bay Voltex MCHT100, was used to provide a 159 kPa and flow rate of 4.73 L/min for around 2.36 L/min through each assembly at a temperature setpoint of 19 °C. The pressure includes the length of hose to and from the coils and the 7.9 mm (inner diameter 5.46 mm) copper tubing of the coil assemblies, which was around 4 m per assembly, quick connect fittings, and an inline filter.

The measured data from the duration test are summarized in Fig. 25. As seen, the dc/dc efficiency during the test dropped slightly from 97.3% to 97.2% over the 20 min interval. At the 50 kW test point, the ferrite, capacitor, and wire losses between GA and VA together are modeled to be 225, 229, and 668 W, respectively, for a total of 1.1 or 0.55 kW per assembly with 112.5 W of ferrite loss and 334 W of wire loss per assembly. The total measured coil–coil loss from the power analyzer was

TABLE XI
MEASURED RMS STRAY FIELD (B_x, B_y, B_z) OF THE GEN. 2 DEMONSTRATOR AT 80 CM AT AN AIRGAP OF 125 MM

Alignment (X,Y)	Measurement Output Power	X-axis (Scaled to 120 kW)	X-axis Vector Sum (Scaled to 120 kW)	Y-axis (Scaled to 120 kW)	Y-axis Vector Sum (Scaled to 120 kW)
(0 cm, 0 cm)	49.0 kW	1.11 µT, 1.51 µT, 1.05 µT (1.74 µT, 2.36 µT, 1.64 µT)	2.15 µT (3.36 µT)	0.36 µT, 1.04 µT, 1.14 µT (0.56 µT, 1.63 µT, 1.78 µT)	1.58 µT (2.48 µT)
(5 cm, 0 cm)	49.0 kW	1.09 µT, 1.88 µT, 1.26 µT (1.71 µT, 2.94 µT, 1.97 µT)	2.51 µT (3.93 µT)	0.40 µT, 1.13 µT, 1.17 µT (0.63 µT, 1.77 µT, 1.83 µT)	1.68 µT (2.62 µT)
(10 cm, 0 cm)	47.4 kW	0.96 µT, 2.92 µT, 1.55 µT (1.53 µT, 4.65 µT, 2.47 µT)	3.44 µT (5.48 µT)	0.70 µT, 1.52 µT, 1.39 µT (1.11 µT, 2.42 µT, 2.21 µT)	2.18 µT (3.46 µT)
(0 cm, 5 cm)	45.9 kW	1.20 µT, 1.65 µT, 1.18 µT (1.94 µT, 2.67 µT, 1.91 µT)	2.36 µT (3.81 µT)	0.57 µT, 1.51 µT, 1.51 µT (0.92 µT, 2.44 µT, 2.44 µT)	2.21 µT (3.57 µT)
(10 cm, 5 cm)	53.9 kW	1.41 µT, 3.86 µT, 1.98 µT (2.10 µT, 5.76 µT, 2.95 µT)	4.56 µT (6.80 µT)	1.06 µT, 2.58 µT, 2.09 µT (1.58 µT, 3.85 µT, 3.12 µT)	3.49 µT (5.20 µT)

Misalignment toward probes.

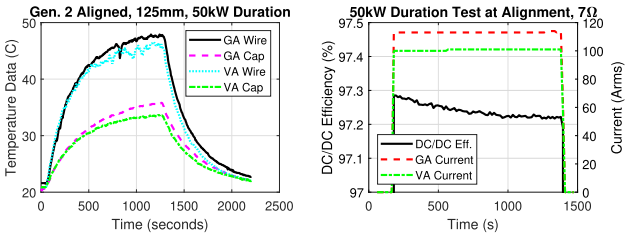

(a) (b)

Fig. 25. Measurements of the Gen. 2 demonstrator from the 50 kW, 20-min duration test with the 2X Inverter. Power transfer starts at the 60 s mark. (a) Measured wire and capacitor temperatures during the test. (b) Measured dc/dc efficiency and GA and VA currents during the test.

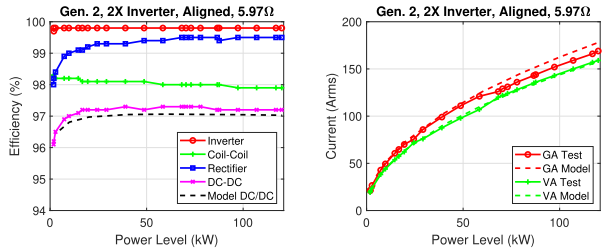

(a) (b)

Fig. 26. Testing of the Gen. 2 demonstrator at alignment and 125 mm with the 2X Inverter. (a) Efficiency breakdown versus output power. (b) Measured versus modeled GA and VA current.

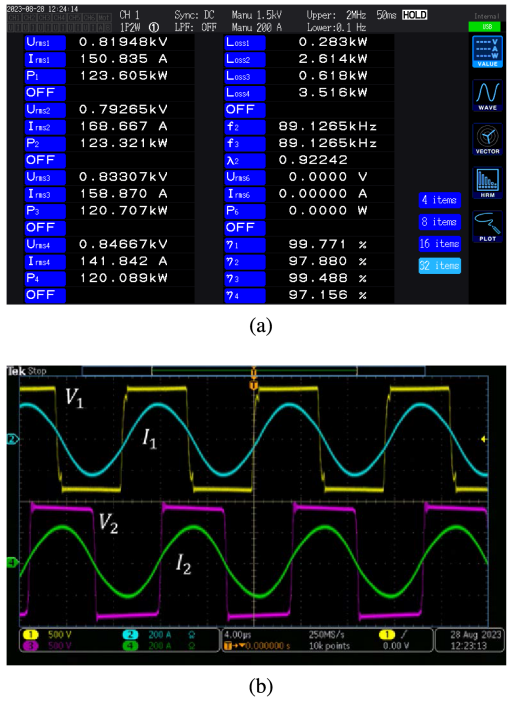

(a)

(b)

Fig. 27. Measurements of the Gen. 2 demonstrator at alignment with a 125 mm airgap at an output power of 120 kW with the 2X Inverter. (a) Power analyzer screenshot and (b) waveforms.

1.0 kW. A measured wire temperature rise of around 27.5°C at the center of both the GA and VA windings relates to between 0.060 K/W at the center of the coil geometry where the temperatures were measured. This is much greater than the FEA simulation in Fig. 11 where an assumed 1200 W of wire loss and 800 W of ferrite loss caused a 45 K wire temperature rise in the center of the geometry, around 0.023 K/W. However, it is also seen that the capacitor temperatures rise around 15 K during the test. The capacitors are mounted and compressed to the surface of the aluminum enclosure on top of 2 mm silicone thermal pads. From the datasheet values, the thermal resistance of the capacitors to the GA and VA aluminum enclosure would be 0.021 K/W, relating to only around 2.5 K of temperature rise from the heat of the capacitors themselves. The rest of the temperature rise of around 12.5 K may come from the rise in the aluminum enclosure temperature. With this adjustment, the rise in temperature relative to enclosure temperature would be around 0.033 K/W at the center of the coil geometry, closer to the modeled value.

A final sweep up to 120 kW was performed with the 2X Inverter to demonstrate the highest efficiency at full power. The efficiency sweep is given in Fig. 26 while the power analyzer screenshot and waveform are in Fig. 27. A dc/dc efficiency of 97.15% was measured at 120.1 kW.

3) Gen. 2 Stray Field Measurements: Stray field measurements were taken during operation with the same NARDA EHP-200 A probe used in the Gen. 1 field measurements. In Table XI, the measured fields at 80 cm at the fundamental are summarized and scaled to a common reference power level of 120 kW for comparison. All of these tests were performed at similar power levels and were taken at a distance of 80 cm away from the center of the GA at the middle of the airgap between the GA and VA. As expected, the stray fields increase with

TABLE XII
MEASURED RMS STRAY FIELD (B_x, B_y, B_z) OF THE GEN. 2 DEMONSTRATOR AT 80 CM AT 125 MM AIRGAP AT ALIGNMENT AT DIFFERENT POWERS

Alignment (X,Y)	Measurement Output Power	X-axis (Scaled to 120 kW)	X-axis Vector Sum (Scaled to 120 kW)	Y-axis (Scaled to 120 kW)	Y-axis Vector Sum (Scaled to 120 kW)
(0 cm, 0 cm)	48.9 kW	0.81 µT, 2.04 µT, 0.88 µT (1.27 µT, 3.20 µT, 1.38 µT)	2.36 µT (3.71 µT)	0.48 µT, 1.80 µT, 1.24 µT (0.75 µT, 2.82 µT, 1.94 µT)	2.24 µT (3.50 µT)
(0 cm, 0 cm)	73.0 kW	1.02 µT, 2.39 µT, 1.03 µT (1.31 µT, 3.06 µT, 1.32 µT)	2.80 µT (3.58 µT)	0.57 µT, 2.18 µT, 1.47 µT (0.73 µT, 2.80 µT, 1.88 µT)	2.69 µT (3.45 µT)
(0 cm, 0 cm)	97.3 kW	1.17 µT, 2.77 µT, 1.18 µT (1.30 µT, 3.08 µT, 1.31 µT)	3.23 µT (3.59 µT)	0.74 µT, 2.76 µT, 1.77 µT (0.82 µT, 3.07 µT, 1.97 µT)	3.36 µT (3.74 µT)
(0 cm, 0 cm)	120.1 kW	1.02 µT, 2.93 µT, 1.27 µT	3.35 µT	0.78 µT, 2.86 µT, 1.83 µT	3.48 µT

misalignment, and especially when the misalignment places the probe closer to the VA. The highest stray field was in the worst-case misalignment (10 cm, 5 cm) measured on the *X*-axis at a vector sum of 4.56 μT(rms) at 53.9 kW output power, or 6.80 μT(rms) when scaled to 120 kW. Later in the tests with the 2X Inverter, a second series of stray field measurements was taken to validate the scaling of field with power level. The measurements, as summarized in Table XII, show consistent scaling of the stray field with power level.

The measured stray field of the Gen. 2 demonstrator was lower than the Gen. 1 demonstrator and very low compared to previous work. As summarized in Table I, with an airgap to GML of 0.262 at an airgap of 125 mm, the measured stray field magnitude at 80 cm is 3.4 μT(rms) and 3.5 μT(rms) on the *X*- and *Y*-axes, respectively, leading to stray field to power level ratios of 3.2 $kW^{0.5}/\mu$T(rms) and 3.1 $kW^{0.5}/\mu$T(rms). Even at maximum misalignment the Gen. 2 system achieves ratios of 1.5 $kW^{0.5}/\mu$T(rms) and 1.9 $kW^{0.5}/\mu$T(rms), easily meeting the 27 μT(rms) ICNIRP limit.

V. CONCLUSION

In this work, a shielded bipolar geometry generated by the FAM optimization was used in the design of a 120 kW proof-of-concept demonstrator to validate a FAM-generated coil geometry in an efficient, low stray field, and high-power system. This validates the FAM approach for different design inputs and at much higher power levels. Using the FAM optimization geometry output, the number of turns, wire, and ferrite were selected, and the physical design was performed to realize a liquid cooled, high-power demonstrator. Several implementation improvements are explored in a Gen. 2 demonstrator with lower encapsulation stress [30], a single passthrough to reduce circulating flux, and improved ferrite layout. The Gen. 2 demonstrator was tested up to 120 kW and demonstrated very low stray field at high power levels and achieved a dc/dc efficiency of 97.2% at 120 kW at alignment with a 125 mm airgap matching the modeled values. At 120 kW near unity gain, the measured stray field magnitudes at 80 cm were 3.4 μT(rms) and 3.5 μT(rms) on the *X*- and *Y*-axes, respectively, well below the 27 μT(rms) ICNIRP stray field limit. The Gen. 2 demonstrator coil area of 42.0 cm $\times$ 54.0 cm and weight of 29.3 kg result in power densities of 530 kW/m^2 and 4.1 kW/kg, respectively, higher than the literature systems reviewed in Table I. All testing was done under soft-switching conditions up to unity gain. To further develop this demonstrator in future work, integration with a dc/dc converter on the output is needed with additional validation at mismatched loading.

ACKNOWLEDGMENT

This work made use of the Engineering Research Center Shared Facilities supported by the Engineering Research Center Program of the National Science Foundation and DOE under NSF Award Number EEC-1041877 and the CURENT Industry Partnership Program. Any opinions, findings and conclusions or recommendations expressed in this material are those of the authors and do not necessarily reflect those of the National Science Foundation. Any opinions, findings and conclusions or recommendations expressed in this material are those of the authors and do not necessarily reflect those of the National Science Foundation.

This research used the resources available at the Power Electronics and Electric Machinery Research Center at the National Transportation Research Center, a US Department of Energy (DOE) Office of Energy Efficiency and Renewable Energy user facility operated by Oak Ridge National Laboratory (ORNL).

This article has been co-authored by Oak Ridge National Laboratory, operated by UT Battelle, LLC, under Contract No. DE-AC05-00OR22725 with the U.S. Department of Energy. The publisher, by accepting the article for publication, acknowledges that the United States Government retains a non-exclusive, paid up, irrevocable, world-wide license to publish or reproduce the published form of this manuscript, or allow others to do so, for United States Government purposes. The Department of Energy will provide public access to the results of federally sponsored research in accordance with the DOE Public Access Plan (http://energy.gov/downloads/doe-public access-plan).

REFERENCES

[1] A. Foote and O. C. Onar, "A review of high-power wireless power transfer," in *Proc. 2017 IEEE Transp. Electrific. Conf. Expo (ITEC)*, 2017, pp. 234–240.

[2] C. C. Mi, G. Buja, S. Y. Choi, and C. T. Rim, "Modern advances in wireless power transfer systems for roadway powered electric vehicles," *IEEE Trans. Ind. Electron.*, vol. 63, no. 10, pp. 6533–6545, Oct. 2016.

[3] D. Patil, M. K. McDonough, J. M. Miller, B. Fahimi, and P. T. Balsara, "Wireless power transfer for vehicular applications: Overview and challenges," *IEEE Trans. Transport. Electrific.*, vol. 4, no. 1, pp. 3–37, Mar. 2018.

[4] M. Hackmann, "P3 charging index report 07/22–Comparison of the fast charging capability of various electric vehicles," P3 Group, 2022. [Online]. Available: https://www.p3-group.com/en/p3-charging-index-comparison-of-the-fast-charging-capability-of-various-electric-vehicles-from-a-users-perspective_07-22/

[5] *J2954: Wireless Power Transfer for Light-Duty Plug-In/Electric Vehicles and Alignment Methodology*, *Soc. Automot. Eng.*, 2022.
[6] International Commission on Non-Ionizing Radiation Protection, "Guidelines for limiting exposure to time-varying electric and magnetic fields (1 Hz to 100 kHz)," *Health Phys.*, vol. 99, no. 6, pp. 818–836, 2010.
[7] *CISPR 11: Industrial Scientific and Medical Equipment - Radio-Frequency Disturbance Characteristics - Limits and Methods of Measurement*, IEC, Geneva, Switzerland, Jun. 2016.
[8] J. Schneider et al., "Validation of wireless power transfer up to 11 kW based on SAE J2954 with bench and vehicle testing," SAE Technical Paper, 2019-01-0868, 2019.
[9] S. Zimmer, M. Helwig, P. Lucas, A. Winkler, and N. Modler, "Investigation of thermal effects in different lightweight constructions for vehicular wireless power transfer modules," *World Electric Veh. J.*, vol. 11, no. 4, 2020, Art. no. 67.
[10] B. Zhang et al., "Multiobjective thermal optimization based on improved analytical thermal models of a 30-kW IPT system for EVs," *IEEE Trans. Transport. Electrific.*, vol. 9, no. 1, pp. 1910–1926, Mar. 2023.
[11] V. P. Galigekere et al., "Design and implementation of an optimized 100 kW stationary wireless charging system for EV battery recharging," in *Proc. IEEE Energy Convers. Congr. Expo. (ECCE)*, 2018, pp. 3587–3592.
[12] K. Askley, "ORNL demonstrates 120-kilowatt wireless charging for vehicles," Oct. 2018. [Online]. Available: https://www.ornl.gov/news/ornl-demonstrates-120-kilowatt-wireless-charging-vehicles
[13] S. Bandyopadhyay, J. Dong, L. Ramirez-Elizondo, and P. Bauer, "Determining relation between size of polarized inductive couplers and nominal airgap," in *Proc. 2018 IEEE 18th Int. Power Electron. Motion Control Conf. (PEMC)*, 2018, pp. 248–255.
[14] A. L. Stein, P. A. Kyaw, and C. R. Sullivan, "Figure of merit for resonant wireless power transfer," in *Proc. 2017 IEEE 18th Workshop Control Model. Power Electron. (COMPEL)*, 2019, pp. 1–7.
[15] M. Mohammad, O. C. Onar, V. P. Galigekere, G. J. Su, and J. Wilkins, "Magnetic shield design for the Double-D coil-based wireless charging system," *IEEE Trans. Power Electron.*, vol. 37, no. 12, pp. 15740–15752, Dec. 2022.
[16] R. Bosshard, "Multi-objective optimization of inductive power transfer systems for EV charging," Ph.D. dissertation, Dept. Inf. Technol. Elect. Eng., ETH Zurich, Zürich, Switzerland, 2015.
[17] R. Bosshard, U. Iruretagoyena, and J. W. Kolar, "Comprehensive evaluation of rectangular and double-D coil geometry for 50 kW/85 kHz IPT system," *IEEE Trans. Emerg. Sel. Topics Power Electron.*, vol. 4, no. 4, pp. 1406–1415, Dec. 2016.
[18] A. Ridge, K. K. Ahamad, R. McMahon, and J. Miles, "Development of a 50 kW wireless power transfer system," in *Proc. 2019 IEEE PELS Workshop Emerg. Technol.: Wireless Power Transfer (WoW)*, 2019, pp. 406–409.
[19] R. Nimri et al., "Hardware considerations of an inductive power transfer pad for heavy-duty electric vehicle charging," in *Proc. 2022 Wireless Power Week (WPW)*, 2022, pp. 705–710.
[20] P. A. J. Lawton, F. J. Lin, and G. A. Covic, "Magnetic design considerations for high-power wireless charging systems," *IEEE Trans. Power Electron.*, vol. 37, no. 8, pp. 9972–9982, Aug. 2022.
[21] J. Pries, V. P. N. Galigekere, O. C. Onar, and G.-J. Su, "A 50-kW three-phase wireless power transfer system using bipolar windings and series resonant networks for rotating magnetic fields," *IEEE Trans. Power Electron.*, vol. 35, no. 5, pp. 4500–4517, May 2020.
[22] M. Mohammad, J. L. Pries, O. C. Onar, V. P. Galigekere, G. J. Su, and J. Wilkins, "Comparison of magnetic field emission from unipolar and bipolar coil-based wireless charging systems," in *Proc. 2020 IEEE Transp. Electrific. Conf. Expo (ITEC)*, 2020, pp. 1201–1207.
[23] A. Foote, D. Costinett, R. Kusch, M. Mohammad, and O. Onar, "Fourier analysis and loss modeling for inductive wireless electric vehicle charging with reduced stray field," *IEEE Trans. Transport. Electrific.*, early access, Feb. 7, 2024, doi: 10.1109/TTE.2024.3363612.
[24] T. Campi, S. Cruciani, F. Maradei, and M. Feliziani, "Active coil system for magnetic field reduction in an automotive wireless power transfer system," in *Proc. 2019 IEEE Int. Symp. Electromagn. Compat., Signal Power Integrity (EMC SIPI)*, 2019, pp. 189–192.
[25] M. Lu and K. D. T. Ngo, "Circuit models and fast optimization of Litz shield for inductive-power-transfer coils," *IEEE Trans. Power Electron.*, vol. 34, no. 5, pp. 4678–4688, May 2019.
[26] E. A. Jones, "Review and characterization of gallium nitride power devices," Masters Thesis, University of Tennessee, Knoxville, Tennessee, 2016.
[27] D. Costinett, D. Maksimovic, and R. Zane, "Circuit-oriented treatment of nonlinear capacitances in switched-mode power supplies," *IEEE Trans. Power Electron.*, vol. 30, no. 2, pp. 985–995, Feb. 2015.
[28] M. Mohammad, S. Choi, Z. Islam, S. Kwak, and J. Baek, "Core design and optimization for better misalignment tolerance and higher range of wireless charging of PHEV," *IEEE Trans. Transport. Electrific.*, vol. 3, no. 2, pp. 445–453, Jun. 2017.
[29] D. E. Gaona-Erazo, C. Jiang, and T. Long, "Highly efficient 11.1 kW wireless power transfer utilizing nanocrystalline ribbon cores," *IEEE Trans. Power Electron.*, vol. 36, no. 9, pp. 9955–9969, Sep. 2021.
[30] A. Foote, D. Costinett, W. Henken, R. Kusch, M. Mohammad, and O. Onar, "Encapsulation residual stress and ferrite loss in inductive coil assemblies," in *Proc. 2023 IEEE Energy Convers. Congr. Expo. (ECCE)*, 2023, pp. 1843–1850.
[31] V. Tsakaloudi, D. Holz, and V. Zaspalis, "The effect of externally applied uniaxial compressive stress on the magnetic properties of power MnZn-ferrites," *J. Mater. Sci.*, vol. 48, no. 10, pp. 3825–3833, 2013.
[32] I. M. Daniel, O. Ishai, I. M. Daniel, and I. Daniel, *Engineering Mechanics of Composite Materials*. New York, NY, USA: Oxford Univ. Press, 2006.
[33] L. Xue et al., "Design and analysis of a 200 kW dynamic wireless charging system for electric vehicles," in *Proc. 2022 IEEE Appl. Power Electron. Conf. Expo. (APEC)*, 2022, pp. 1096–1103.
[34] K. Aditya and S. S. Williamson, "Design guidelines to avoid bifurcation in a series–series compensated inductive power transfer system," *IEEE Trans. Ind. Electron.*, vol. 66, no. 5, pp. 3973–3982, May 2019.

Andrew Foote (Member, IEEE) received the B.S. degree in electrical engineering from Auburn University, Auburn, AL, USA, in 2016, and the Ph.D. degree in electrical engineering from the University of Tennessee, Knoxville, Knoxville, TN, USA, in 2023.

From 2016 to 2019, he joined the Power Electronics and Electric Machinery Group at Oak Ridge National Laboratory, Oak Ridge, TN, as a Graduate Research Assistant. In 2020, he joined the Volkswagen Group of America at Innovation Hub Knoxville, Oak Ridge, as part of the first cohort of Ph.D. Fellows and transitioned to working as a Research Engineer there in November 2023. His research interests include the design and optimization of inductive wireless charging assemblies, magnetic components, resonant tank elements, thermal management, power electronic converters, and electric machines and drives for electric vehicles.

Daniel Costinett (Senior Member, IEEE) received the Ph.D. degree in electrical engineering from the University of Colorado Boulder, Boulder, CO, USA, in 2013.

In 2013, he was an Instructor at Utah State University, Logan, UT, USA. Since 2013, he has been with the Department of Electrical Engineering and Computer Science, University of Tennessee, Knoxville (UTK), Knoxville, TN, USA, where he is currently an Associate Professor. He is Co-Director of Education and Diversity for the National Science Foundation/Department of Energy Engineering Research Center for Ultra-wide-area Resilient Electric Energy Transmission Networks (CURENT). He has coauthored more than 150 peer-reviewed publications. His research interests include resonant and soft switching power converter design, high efficiency wired and wireless power supplies, on-chip power conversion, medical devices, and electric vehicles.

Dr. Costinett was the recipient of the National Science Foundation CAREER Award in 2017, the 2022 Richard M. Bass Outstanding Young Power Electronics Engineer Award, the 2016 and 2020 IEEE PELS Transactions Second Place Prize Paper Award, the 2015 IEEE IAS William M. Portnoy Award, the 2022 Moses E. and Mayme Brooks Distinguished Professor Award, 2015 ECE Faculty of the Year Award, and 2020 Chancellor's Award for Professional Promise in Research from UTK. He is currently the Associate Editor of IEEE TRANSACTIONS ON POWER ELECTRONICS.

Ruediger S. Kusch (Senior Member, IEEE) received the Dipl.-Ing. degree in electrical engineering from the Braunschweig University of Technology, Braunschweig, Germany, in 1998, and the Ph.D. degree in electrical engineering from the Berlin University of Technology, Berlin, Germany, in 2006.

From 1998 to 2000, he was with the Fraunhofer Institute for Applied Research. In 2001/02, he was a Research Scholar at the Department of Electrical and Computer Engineering, University of Wisconsin (WEMPEC), Madison, Madison, WI, USA. From 2006 to 2013, he was with General Electric Global Research, Niskayuna, NY, USA. He is currently a Senior Engineer with Volkswagen R&D, Wolfsburg, Germany. He holds 52 patents. His research interests include electric machines, drives and their control, electrification of the vehicle drive train, wide bandgap semiconductors, power conversion, electric vehicles, battery management systems, fuel cell systems, more electric aircraft, medium voltage drives, solid state transformer, power converter topologies, and high bandwidth control.

Mostak Mohammad (Senior Member, IEEE) received the B.Sc. degree in 2009 in electrical and electronics engineering from the Bangladesh University of Engineering and Technology (BUET), Dhaka, Bangladesh, and the Ph.D. degree in electrical engineering from the University of Akron, Akron, OH, USA, in 2019.

From 2009 to 2014, he worked as a specialist in Radio Network Planning in Robi Axiata Limited, Dhaka where he developed radio-frequency propagation models for FEA-based cellular network design. He is currently working as an R&D Associate Staff with the National Transportation Research Center, Oak Ridge National Laboratory, Oak Ridge, TN, USA. He has been working on high-power (11–500 kW) single-phase, poly-phase, stationary and dynamic wireless charging systems. His research interests include high-fidelity multiphysics modeling and optimization, high-power wireless charging for electric vehicles, magnetic materials, electromagnetic shielding, and electric machine design.

Omer Onar (Senior Member, IEEE) received the Ph.D. degree in electrical engineering from the Illinois Institute of Technology, Chicago, IL, USA, in 2010.

In 2010, he joined the Power Electronics and Electric Machinery Group at the U.S. Department of Energy's Oak Ridge National Laboratory, Oak Ridge, TN, USA, as a Distinguished Alvin M. Weinberg Fellow. He is currently leading the Vehicle Power Electronics Research (VPER) Group under the Vehicle and Mobility Systems Research Section, Buildings and Transportation Science Division. His research interests include power electronic converters for EV charging applications, wireless power transfer systems, bidirectional EV charging systems, and drive systems.